

Smoothed Particle Hydrodynamics Simulations for Dynamic Capillary Interactions

By

Yanyao Bao

A thesis submitted in fulfilment of the requirements for the degree of

Master of Philosophy

Faculty of Engineering and Information Technology

The University of Sydney

2018

Acknowledgements

First of all, I would like to express sincere appreciation to my supervisor Dr. Yixiang Gan for accepting me as his student and providing helpful discussion and direction throughout this project. I'm always feeling supported and inspired by his insightful advice and outstanding expertise, working under his supervision has significantly shaped my own conduct and practices in academic research.

I would like to express my thanks to Dr. Ling Li, for introducing me to the world of SPH and for his patient and thoughtful guidance throughout this work. I also want to thank my co-supervisor, A/Prof. Luming Shen, for his critical comments and feedbacks which greatly improved the quality of my research and manuscript.

I would like to thank all the group members for the friendly and helpful working environment they have provided. I especially want to thank Dr. Chongpu Zhai, Mr. Weijing Dai, Mr. Zhang Shi, Mr. Mingrui Dong, Mr. Zhongzheng Wang, Mr. Guanzhe Cui, and Mr. Pengyu Huang for their comments and suggestions on my work. In addition, I want to thank Mr. Bowei Yu, Ms. Karina Arias Calluari, Ms. Man Xu, and all the friends in the office for their encouragement and company.

I dedicate this thesis to my family and my wife, Baowen Zhang, for all the love and support.

Notation

The following is a list of the symbols used in this thesis.

γ	Interfacial tension (mN/m)
P	Pressure (Pa)
R	Radius of meniscus curvature (mm)
θ	Contact angle (°)
θ_a	Advancing angle (°)
θ_r	Receding angle (°)
θ_d	Dynamic contact angle (°)
θ_s	Quasi-static contact angle (°)
ρ	Density (kg/m ³)
g	Gravity (m/s ²)
l_c	Capillary length (mm)
b	Characteristic length (mm)
L_s	Slip length (mm)
η	Viscosity (Pa·s)
Ca	Capillary number
A, B	Constants in power law function
ω	Liquid bridge transfer ratio
U	Substrate stretching speed (cm/s)
\mathbf{r}	Position vector of SPH particle
h	Smoothing length (m)

m	Particle mass (kg)
W	Smoothing function
c	Artificial sound speed (m/s)
Δt	Time step (s)
C, D	Constants in potential energy function
α_{ij}	Inter-particle force strength parameter (J)
τ	Shear stress (N/m ²)
$\dot{\gamma}$	Shear rate (s ⁻¹)
L_0	Particle spacing (m)
\mathbf{F}_i^{vis}	Interfacial viscous force (N)
η^*	Interfacial viscosity (Pa·s)
Q	Flow rate (m ³ /s)
v_t	Triple-line region velocity (m/s)
t	Simulation time (ms)
θ_t	Contact angle of top substrate (°)
θ_b	Contact angle of bottom substrate (°)

Abstract

Complex interactions in porous media play an important role on many industrial and geotechnical applications, such as groundwater treatment, porous catalysts, carbon geosequestration, and oil recovery. Rate-dependent wetting effects are of great significance in understanding the multiphase behaviours of porous media thus further throw light on engineering solutions to the above problems. A number of experimental studies and theoretical models suggest that the contact angle varies with the velocity of fluid at triple-line region, thus resulting in dynamic capillary interactions.

In this thesis, a modified smoothed particle hydrodynamics (SPH) model is applied to simulate (1) the contact angle dynamics and (2) stretching of liquid bridge at meso-scale. This SPH model adopted an inter-particle force formulation with short-range repulsive force and long-range attractive force to take into account single-phase and multiphase interactions. The free surface of fluids with different surface tension can be reproduced by adjusting liquid-liquid inter-particle force parameter. By changing the liquid-solid inter-particle force parameter, solid surfaces from hydrophobicity to hydrophilicity can be reproduced. Through parametric studies, other physical properties predicted from the model including density, viscosity and compressibility are also implemented and can be altered for various fluid constituents. Particularly, a newly-introduced viscous force is imposed at the liquid-solid interface to capture the rate-dependent behaviours of contact angle without prescribing additional arbitrary condition or force.

After identification of model parameters in Chapter 4, the rate-dependent contact angle behaviours are studied in Chapter 5, for both wetting and dewetting phenomena. It has been found that the dynamic contact angle only occurs when the proposed interfacial viscous force is included in the momentum equation. By analysing the contact angle results of fluid at triple-line region with different moving speeds, the dynamic contact angles and corresponding capillary numbers can be correlated by power law functions. The derived correlation and constants are compared with different forms of empirical power law functions and the results are satisfactory. The magnitude of interfacial viscous force is proven to be influential on contact angle dynamics, and this interfacial model shares direct physical links with the apparent slip length and microscopic surface roughness.

In Chapter 6, we investigated the properties of stretching liquid bridges, including shape evolution, liquid transfer ratio and flow condition under dynamic loading. The Equation of State is modified for reproducing the rupture of a stretched liquid bridge. Different stretching rates are applied, and the shapes of liquid bridge at same breakup distance is presented. By differentiating the wettability of top and bottom substrates, the liquid transfer ratio regarding wettability difference and substrate moving speed is studied. In addition, we examined the flow condition during liquid bridge formation and rupture.

In conclusion, a modified SPH model has been proposed to simulate the pore-scale effects and interactions, including surface tension, dynamic contact angles, and stretching of liquid bridges. With the newly-introduced interfacial viscous force which accounts for the relative shearing between solid and liquid particles, the contact angle associated with a moving contact line can be successfully reproduced. In addition, the shape evolution and rupture of liquid bridge are further studied by setting different stretching speeds and wettability of substrates. These results demonstrated the robustness of the proposed model in simulating multiphase flow in geo-materials, and the potential to interpret more complex characteristics and behaviours of capillary interactions at macro-scale.

Contents

ACKNOWLEDGEMENTS	I
NOTATION	II
ABSTRACT	IV
CHAPTER 1 INTRODUCTION	1
CHAPTER 2 LITERATURE REVIEW	5
2.1 CAPILLARY INTERACTIONS	5
2.1.1 SURFACE TENSION	5
2.1.2 YOUNG-LAPLACE EQUATION	6
2.1.3 CAPILLARY PRESSURE	6
2.1.4 CAPILLARY LENGTH	7
2.1.5 BOUNDARY CONDITION AND SLIP LENGTH	7
2.2 CONTACT ANGLE HYSTERESIS AND DYNAMICS	9
2.2.1 WETTING AND CONTACT ANGLE	9
2.2.2 RATE-DEPENDENT BEHAVIOUR OF CONTACT ANGLE	10
2.2.3 MEASUREMENT OF CONTACT ANGLE	11
2.3 STRETCHED LIQUID BRIDGES	12
2.3.1 CAPILLARY FORCE	12
2.3.2 LIQUID TRANSFER	12
2.4 SPH METHODS FOR CAPILLARY INTERACTIONS	14
2.4.1 ADVANTAGES AND DISADVANTAGES OF SPH METHODS	15
2.4.2 IMPLEMENTATION OF SURFACE TENSION IN SPH	16
2.4.3 PRESCRIBING DYNAMIC CONTACT ANGLE IN SPH	17
CHAPTER 3 SPH METHOD AND NUMERICAL MODEL	19
3.1 SPH METHOD	19
3.1.1 SMOOTHING FUNCTION	19

3.1.2 APPROXIMATION OF THE FUNCTION'S GRADIENT	20
3.1.3 FORMS OF SMOOTHING FUNCTIONS	20
3.2 NUMERICAL MODEL	21
3.2.1 MOMENTUM EQUATION	21
3.2.2 CONTINUITY EQUATION	22
3.3.3 EQUATION OF STATE (EOS)	22
3.3.4 ARTIFICIAL VISCOSITY	23
3.3.5 XSPH CORRECTION	24
3.3.6 TIME INTEGRATION	24
3.3 INTER-PARTICLE FORCE MODEL IN SPH	25
3.4 INTERFACIAL VISCOUS FORCE FORMULATION	26
 CHAPTER 4 IDENTIFICATION OF MODEL PARAMETERS	 30
 4.1 DENSITY AND PRESSURE	 30
4.2 VISCOSITY MEASUREMENT	32
4.3 SURFACE TENSION	34
4.4 CONTACT ANGLE	36
4.5 BOUNDARY CONDITION EXAMINATION	38
 CHAPTER 5 DYNAMIC CONTACT ANGLE	 41
 5.1 SIMULATION GEOMETRY AND SETUP	 41
5.2 EFFECTIVENESS TEST FOR <i>Fivis</i>	43
5.3 PARAMETRIC STUDY OF η^*	46
5.4 SCALING OF η^*	51
5.5 MESH SENSITIVITY TEST FOR <i>Fivis</i>	52
5.6 VELOCITY FIELD IN CAPILLARY TUBES	53
5.7 SUMMARY	56
 CHAPTER 6 DYNAMIC BEHAVIOUR OF STRETCHING LIQUID BRIDGES	 58
 6.1 A MODIFIED EOS FOR LIQUID RUPTURE	 58
6.2 RATE-DEPENDENT BEHAVIOUR OF A STRETCHING LIQUID BRIDGE	62
6.3 FLOW CONDITION IN LIQUID BRIDGES	65

6.4 SUMMARY	66
<u>CHAPTER 7 CONCLUSION AND FUTURE WORK</u>	<u>68</u>
7.1 CONCLUSION	68
7.2 FUTURE WORK	69
<u>REFERENCES</u>	<u>72</u>
<u>APPENDIX A: 2D HAGEN–POISEUILLE EQUATION DERIVATION</u>	<u>78</u>
<u>APPENDIX B: IMAGE PROCESSING FOR CONTACT ANGLE FITTING</u>	<u>80</u>
<u>APPENDIX C: LIQUID PARTICLE COUNTING</u>	<u>81</u>

Chapter 1

Introduction

Multiphase flows and capillary interactions in porous media are of great significance in many industrial applications, such as carbon sequestration [1], groundwater treatment [2], oil recovery [3], and porous catalysts [4]. These processes usually involve rate-dependent wetting behaviour, which acts as a critical role in describing the wetting and dewetting of the systems. To account for the dynamic wettability and associated contact angle dynamics, experimental characterisation [5-7], theoretical modelling [8, 9], and various numerical methods [10-12] are conducted over the decades. Among these approaches, numerical methods demonstrated substantial advantages in modelling the multiphase flow and capillary interactions, including time and cost efficiency, flexibility of simulation length scales, and free of external interference. However, there are limited cases with successful numerical implementation in modelling the dynamic capillary interactions within reasonable time and length scales while preserving realistic physical basis and quantities.

Contact angle is formed when a liquid is brought into contact with solid surface and it can change considerably from static value under dynamic conditions due to the contact line motion. The dynamic contact angle, θ_d , associated with a moving contact line can be expressed by the corresponding triple-line region velocity v_t and quasi-static contact angle θ_s : $\theta_d = f(v_t, \theta_s)$ [13]. The dynamic contact angle is an important physical parameter in fluid dynamics that affecting the behaviours of capillary flows with low Reynold number, Re . The capillary flows are usually represented by relatively small capillary number, Ca and bond number, Bo :

$$Ca = \frac{\text{viscous force}}{\text{surface tension force}} = \frac{\eta v}{\gamma}, \quad (1.1)$$

$$Bo = \frac{\text{gravitational force}}{\text{surface tension force}} = \frac{g \rho b^2}{\gamma}, \quad (1.2)$$

where ρ , γ , η , v , g and b are density, surface tension, viscosity, velocity, gravity and characteristic length, respectively. To account for the problem of contact angle with moving

contact line, researchers have developed several models including hydrodynamic model [8], molecular-kinetic model [14], and combined model [15].

However, the complete understanding of dynamic contact angle with moving contact line is still an open topic due to the complex multiphase interactions and the fundamental role of the liquid-solid-vapour triple-line region in the liquid spreading. Experimental investigations on dynamic contact angle could be strongly influenced by small length-scale physical and chemical heterogeneities, surface roughness change due to liquid-solid phase interactions, impurities adsorbed on the solid surface, and growth and dissolution of bubbles, etc [16]. Therefore, the numerical modelling of the dynamic contact angle plays a significant role in studying the capillary effects and fluid dynamics.

Considering the above-mentioned limitations and availability of experimental conditions and facilities, the numerical approaches including molecular dynamics (MD) [11, 17, 18], lattice-Boltzman methods (LBM) [10, 19, 20], and smoothed particle hydrodynamics (SPH) [12, 21] serve as powerful tools to study the fundamental mechanisms within capillary interactions. At the micro-scale, Koplik et al. [11] identified rate-dependent behaviour for dynamic receding angle with MD simulation in an immiscible two-fluid system. Lukyanov and Likhtman [18] applied MD simulation to explain the behaviours of dynamic contact angle from the perspective of force distribution and friction law. Nevertheless, there are restrictions in simulation time and length scales due to the high computing power required for MD simulations. At the meso-scale, researchers also proposed and verified the power law correlation between Ca and dynamic contact angle with multiphase capillary flow using LBM and SPH method, and the outcomes consist with experimental results and theoretical predictions [10, 12, 19-21]. To deal with moving boundaries problem, LBM requires additional algorithm which may lose the accuracy of the standard scheme [22]. For the previously mentioned SPH models that successfully simulated the dynamic contact angle, additional terms should be imposed, such as contact line force formulation at the triple-line region [12] and Young–Laplace boundary condition at the fluid-fluid interface [21], all of which require explicit modelling of all phases in the pore space thus dramatically increase the computational cost.

This thesis is organized as follows: In Chapter 2, we present a literature review regarding basic knowledge and current study on dynamic capillary interactions, i.e., (1) contact angle dynamics, and (2) stretching and rupture of liquid bridges. Experimental findings, theoretical predictions and simulation approaches concerning the contact angle with moving contact line problem are

presented and discussed. The SPH model with inter-particle force and modified liquid-solid interface formulation are described in Chapter 3. Chapter 4 presents parameter identification and model calibration for density, viscosity, surface tension, static contact angles and liquid-solid interactions. In Chapter 5, we examine the effectiveness of newly-introduced interfacial viscous force formulation. Then the correlations between dynamic contact angle and Ca with empirical power law functions are analysed under different magnitude of interfacial viscous force. The physical meaning of interfacial viscous force parameter is further illustrated from the perspective of slip length and microscopic surface roughness, followed by mesh sensitivity tests and flow condition examination. Chapter 6 presents the rate-dependent behaviours of liquid bridges under dynamic loading conditions. The shape evolution of liquid bridges with different stretching speeds and substrate wettability are described. In addition, we study the liquid bridge transfer ratio by differentiating the wettability of top and bottom substrates, and the results are compared with other experiments and simulations. Finally, conclusions are made in Chapter 7.

Chapter 2

Literature Review

In this Chapter, the background and basic concepts of capillary interactions will be presented. Based on theoretical predictions, experimental results and numerical simulations, the rate-dependent behaviours of capillary interactions are introduced and discussed with an emphasis on contact angle dynamics and properties of stretched liquid bridges. In addition, a brief introduction of SPH method with existing approaches for surface tension and dynamic contact angle prescription is presented.

2.1 Capillary interactions

2.1.1 Surface tension

Surface tension, caused by the imbalance of molecular force at the interface between two immiscible fluids, is one of the most important properties in the phenomenon of capillarity. In the fluid bulk region, each molecule is pulled equally by neighbouring molecules in every direction, while there is no molecule for those molecules exposed at the surface. Therefore, the force balance is broken at the surface, and this leads to an attractive force pulling the surface inwards to maintain the lowest surface free energy as well as the least surface area of the fluid.

The surface tension is defined as the work consumed (ΔW) per unit of new surface area formed (ΔA) [23]:

$$\gamma = \frac{\Delta W}{\Delta A} = \frac{F \Delta R}{\Delta A} = \frac{F \Delta R}{2\pi R \Delta R} = \frac{F}{2\pi R} = \frac{F}{L}, \quad (2.1)$$

where γ is surface tension, F is the force acting on the surface, R is the droplet circle radius, and L is the length of the line that the force acts on perpendicularly. In practise, surface tension can be measured by several methods such as capillary rise method, sessile drop method, bubble pressure method and so on.

2.1.2 Young-Laplace equation

A consequence of surface tension is the presence of a pressure difference ΔP between a liquid drop and the medium. Considering a small section of the interface between liquid and gas phase, see Fig. 2.1. The surface is expanded by a tiny amount of δz along the normal to the surface, with the local radius of curvature changing from R_i to $R_i + \delta z$, and the area $A = \delta x \delta y$ also increases to $\left(1 + \frac{\delta z}{R_1} + \frac{\delta z}{R_2}\right) A$. In equilibrium, the virtual work done by the contraction forces must balance the work of the pressure:

$$\gamma \left(\frac{1}{R_1} + \frac{1}{R_2} \right) A \delta z - \Delta P \delta V = 0, \quad (2.2)$$

where $\delta V = A \delta z$ is the small change in droplet volume due to the displacement of the interface, and the Young–Laplace equation is derived as:

$$\gamma \left(\frac{1}{R_1} + \frac{1}{R_2} \right) = \Delta P, \quad (2.3)$$

where R_1 and R_2 are the principal radius of curvature.

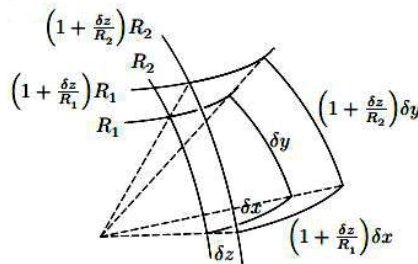


Fig. 2.1 The geometry considered to derive the Young-Laplace equation [24].

2.1.3 Capillary pressure

Capillary pressure acts as dominant role in the displacement of multiphase flow, and it is generally defined as the pressure difference across the interface between two immiscible fluids, see Fig. 2.2 [25]:

$$P_c = P_{nw} - P_w, \quad (2.4)$$

where P_c is capillary pressure, P_{nw} is the pressure in the non-wetting phase and P_w is the pressure in the wetting phase.

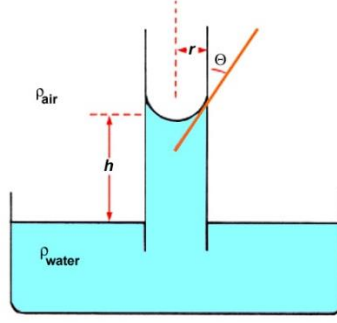


Fig. 2.2 Illustration of capillary pressure: water rise in a capillary tube, where water is a wetting fluid and air is a non-wetting fluid.

According to Young-Laplace equation, the wetting contact angle of free surface inside the capillary tube is prescribed by the capillary pressure, surface tension, and effective radius of curvature [26, 27]:

$$P_c = \frac{2\gamma\cos\theta}{R}, \quad (2.5)$$

where θ is the contact angle on the surface of the capillary and R is the effective radius.

2.1.4 Capillary length

It is common to observe free liquid presenting different rest shapes, because in addition to surface tension, other forces also contribute largely to the overall liquid-air interface shape. The most common factor is gravity, which flattens profile of large drops to reduce the gravitational energy of the liquid. For gravity to be negligible, the radius of the droplet should be smaller than the capillary length l_c , which is defined by the balance between Young-Laplace pressure γ/L and the correspondent hydrostatic pressure ρgL :

$$l_c = \left(\frac{\gamma}{\rho g}\right)^{\frac{1}{2}} \quad (2.6)$$

The capillary length provides a clear upper bound on the size of the systems in the following simulations, as long as we are focusing on capillarity interactions.

2.1.5 Boundary condition and slip length

The physics of the interfacial flow between the liquid and solid phases are critical for in-depth understanding of fluid dynamics in confined geometries. Identifying the appropriate boundary conditions is one of the most important contents in studying the above system. The no-slip boundary condition in Fig. 2.3 (a) is usually considered to be appropriate for most macro flows,

where the relative velocity of fluid adjacent to the solid boundary is assumed to be zero. Other than the no-slip condition, partial slip is first proposed by Navier [28] to describe the slip of fluid at solid surface, as shown in Fig. 2.3 (b). The slip length L_s represents the distance from the liquid-solid interface to the point where the extrapolation of liquid velocity is zero. In Navier's model, slip velocity v_s is related to L_s as well as the shear rate that fluid exert at the wall:

$$v_s = L_s \frac{\partial v_b}{\partial z}, \quad (2.7)$$

where v_b is the velocity of the bulk fluid and z is the axis perpendicular to the wall.

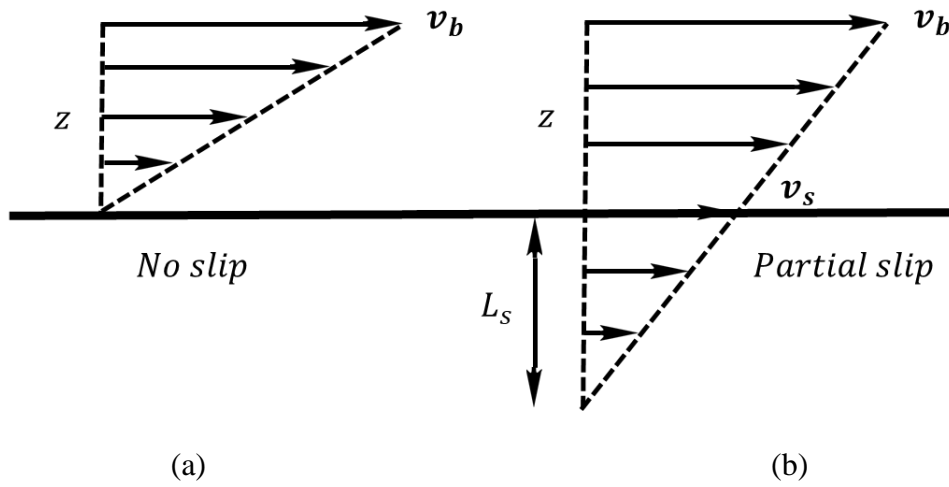


Fig. 2.3 Schematic representation of (a) the no-slip boundary condition, and (b) the partial slip boundary condition.

According to a number of experimental studies, L_s usually ranges from 0 to 10 nm with various fluids and solid surfaces, and some of the cases show dependency of slip on shear rate. More details are described and summarized in [29]. However, compared with the predictions under no-slip boundary conditions and bulk fluid viscosity, the average boundary fluid velocity and slip length of pressure-driven flow can increase dramatically on certain surfaces, such as superhydrophobic and rough surfaces [30-33]. For instance, for hexadecane flowing over a bare sapphire surface, L_s can reach hundreds of nanometres [30], and L_s up to 400 μm was achieved on hydrophobic micro-macro structures [33]. Furthermore, the slip length can even larger than 1 mm for fluid flow through the aligned carbon-nanotube membrane [32]. In addition, molecular dynamics simulations also suggest slip length may increase as the approaching of contact line [11].

2.2 Contact angle hysteresis and dynamics

2.2.1 Wetting and contact angle

Wetting process can be characterised by the liquid-solid-vapour three-phase contact line as a combination consequence of adhesive and cohesive forces. The three-phase contact line generates a contact angle which is regarded as primary parameter in wettability studies. In general, contact angle less than 90° represents high wettability of surface, i.e., hydrophilicity while for the contact angle larger than 90° corresponds to low wettability, i.e., hydrophobicity.

Equilibrium contact angle θ_e is achieved when three-phase contact line no longer moves, see Fig. 2.4, and θ_e relates the relative strength of the liquid, solid, and vapour molecular interaction according to Young's equation [26]:

$$\gamma_{lv}\cos\theta_e = \gamma_{sv} - \gamma_{sl}, \quad (2.8)$$

where γ_{lv} , γ_{sv} and γ_{sl} are the liquid-vapor, solid-vapor and liquid-solid interfacial tension respectively.

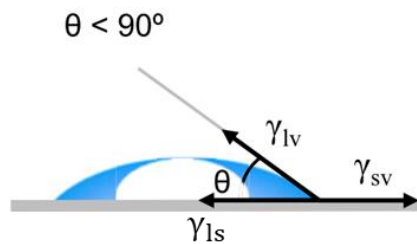


Fig. 2.4 Equilibrium contact angle formed on a smooth homogeneous solid surface [34].

Based on Young's equation, thermodynamic parameters γ_{lv} , γ_{sv} and γ_{sl} give a unique contact angle when the wettability of an ideal surface is fixed. However, on a non-ideal surface, the contact angles formed by expanding or contracting the liquids could be greatly different. These two contact angles are called advancing or receding angle, respectively, which represent the maximum or minimum contact angle when the advancing or receding contact line begin to move, see Fig. 2.5. The difference between the advancing angle θ_a and receding angle θ_r is characterised as contact angle hysteresis [35].

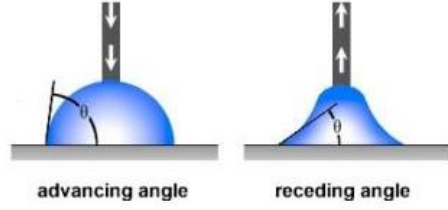


Fig. 2.5 Advancing and receding angles induced by the drop method [25].

2.2.2 Rate-dependent behaviour of contact angle

The apparent contact angle associated with a moving contact line varies with velocity. The behaviours of dynamic contact angle associated with contact line motion of spreading liquids can be described by several theories, including hydrodynamic model [8], molecular-kinetic model [14], and their combination [15]. A number of empirical relationships and theoretical models for wetting have been discussed in the literature, and all of which suggest the dynamic advancing (or receding) contact angle θ_d^a (θ_d^r) as a function of Ca and the corresponding quasi static contact angle θ_s^a (θ_s^r) during wetting (dewetting) processes. Elliot and Riddiford [36] found the dynamic contact angle is rate-independent when $Ca < 2 \times 10^{-7}$ for water with glass or polyethylene plate. Schwartz and Tejada [5] also identified that the dynamic contact angle is constant for $Ca < 2 \times 10^{-6}$. For $10^{-6} < Ca < 10^{-2}$, the dynamic contact angle changes monotonically with Ca , and the most commonly suggested relationship is:

$$|\cos\theta_d^{a/r} - \cos\theta_s^{a/r}| = ACa^B, \quad (2.9)$$

where A and B are constants. This result reveals that dynamic wetting has universal behaviour which is independent of the details of the liquid-solid-gas system [13].

From theoretical predictions and studies, different values for exponent B are derived. Nattermann et al. [37] applied functional renormalization-group (RG) methods to describe the behaviour of depinning transition and obtained $B = 1.5$. Hoffman [9] assumed a microscopic scenario where the liquid molecules advance at liquid-gas interface by a surface diffusion mechanism, and $B = 1$ is obtained over the range of $10^{-5} < Ca < 10^{-3}$. Cox [8] adopted a general slipping model and a matched asymptotic expansion to investigate the contact line movement and obtains $B = 1$ for $Ca < 10^{-3}$. A treatment of the contact line motion in the presence of an adsorbed film is given by Mumley et al. [38], and they obtained $B \approx 0.5$ for $10^{-4} < Ca < 10^{-2}$ and $B \approx 1$ for $Ca < 10^{-5}$. Ishimi et al. [39] considered the complete wetting situation in the presence of a monomolecular film. They presume that the energy dissipation is caused by a frictional force acting on the film due to the balance for interfacial tension forces and the

analysis led to $B = 0.5$. Sheng and Zhou [40] took a different approach and confirmed that viscous effects would give an intrinsic $B = 1$ for relatively small Ca .

In addition to the abovementioned theoretical models, experimental studies with various techniques in diverse systems have also found different values for the exponent B over wide ranges of Ca . Schwartz and Tejada [5] measured the dynamic contact angle by dipping filaments with rough surfaces into different liquids. The results led to $1/3 < B < 1$ for Ca ranging from 10^{-4} to 10^{-2} . Rillaerts and Joos [41] used paraffin oil and aqueous glycerol to measure the dynamic contact angle in prewetted capillaries, and the results suggest that $B = 0.5$ for $4 \times 10^{-4} < Ca < 4 \times 10^{-2}$. Bracke et al. [7] measured dynamic contact angles in which a continuous solid strip is drawn into a large liquid pool. After testing with several liquids including corn oil aqueous, glycerine, and ethyleneglycol solutions, they obtained $B \approx 0.5$ for $3 \times 10^{-3} < Ca < 10^{-1}$. Stokes et al. [42] used a glycerol-methanol mixture as the more wetting fluid to displace a mineral oil. They found $B \approx 0.4$ for $5 \times 10^{-5} < Ca < 5 \times 10^{-4}$. Recently, Zhang et al. [43] Obtained $B \approx 0.2$ for water and glycerol between two moving substrates over the range $10^{-5} < Ca < 10^{-1}$.

It's also been pointed out that the dependence of the contact angle on moving contact line velocity, i.e., the value of B , is enhanced by rough surfaces [5, 44]. Karim et al. [45] conducted dynamic contact angle experiments on rough Teflon plates with different roughness, and they found the dynamic contact angle is significantly influenced by the degree of roughness of Teflon surface. The contact angle hysteresis is only within 5° on smooth surface. While on rough surface, the contact angle hysteresis is more than 20° and increases with the surface roughness.

2.2.3 Measurement of contact angle

One significant challenge with droplets from particle method simulations is that the conventional contact angle becomes ill-defined even for smooth surfaces, as illustrated in Fig. 2.6. Due to the interaction between the surface and the fluid, the liquid particles adjacent to the surface is frequently restructuring. Therefore, different methods to approximately fit the outline of a droplet and measure the contact angle have been applied [46-48]. One approach is to neglect the liquid particles that are closest to the surface for a certain distance [49-51]. This approach is realized by physically drawing a line that is equal to the slope of the droplet just above the neglected thickness, then using this line to calculate the contact angle between the droplet and the surface. This treatment is simple and only requires a liquid density profile and

drawing a line. The disadvantage is the lack of an empirical method to verify the accuracy of the line placement, thus could lead to some error for the calculation of contact angle. Considering the anisotropy of the wetting behaviour, contact angle values are often averaged from different side views.



Fig. 2.6 Illustration of the contact angle measurement deviation [52].

2.3 Stretched liquid bridges

2.3.1 Capillary force

As mentioned in Section 2.1.2, the Young-Laplace equation relates the mean curvature and the pressure difference across the liquid interface. When the liquid bridge is formed between two parallel substrates as shown in Fig. 2.7, the force that the liquid bridge exerts on the substrates can be calculated from the Laplace pressure and the contact area of the liquid on the substrate:

$$F_l = \pi R_1^2 \gamma \left(\frac{1}{R_1} + \frac{2 \cos \theta}{H} \right), \quad (2.10)$$

where F_l is the total force, R_1 and R_2 are the principle radii of the curvature, H is the height of the liquid bridge, and θ is the contact angle.

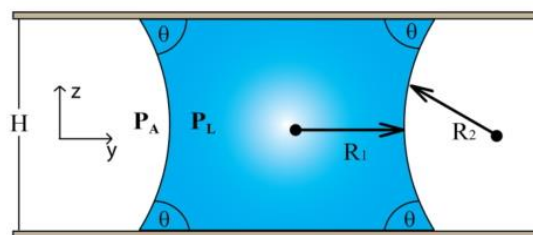


Fig. 2.7 Schematic of a capillary bridge between two parallel plates [53].

2.3.2 Liquid transfer

Liquid bridges formed between two rigid bodies with an arbitrary shape play an important role in capillary interactions. The rupture and transfer of liquid bridge has been widely investigated. A typical transfer process usually involves compress, pause, retreat and rupture, see Fig. 2.8.

With the compress of the substrate, a liquid bridge is formed between the acceptor and donor surfaces. After the system is in the equilibrium state, the acceptor substrate is slowly retreated from the donor surface till the liquid bridge is ruptured. The shape of a stretched liquid bridge has been demonstrated to be affected by various factors, including stretching speed, wettability of substrates, viscosity and surface tension of liquid, etc. [54-56].

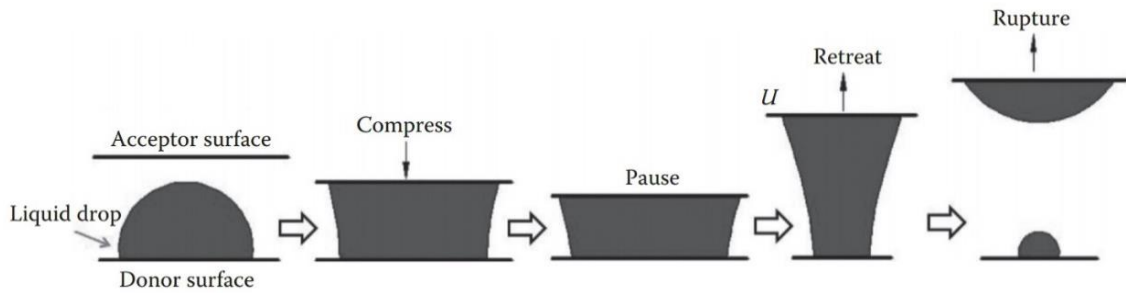


Fig. 2.8 A schematic illustration of a typical liquid drop transfer process [57].

The transfer ratio, ω , is another important parameter in describing the stretching process of a liquid bridge, which is defined as the ratio between the volume of the liquid transferred onto the acceptor surface and the total liquid volume. Experimental findings and theoretical models have demonstrated that the transfer ratio can be described as a function of stretching speed U : $\omega = f(U)$, and three regimes for liquid transfer (quasi-static, transition and dynamic) are identified [57]. In Fig. 2.9, we can see that the transfer ratio is almost 100% for relatively small stretching speed, and this regime refers to the quasistatic regime where surface forces dominates the transfer process. While for relative large stretching speed, the transfer ratio converges to 0.5, and viscous and inertial forces dominate this dynamic regime. In the transition regime, all the three forces are contributing to the transfer process. It is noteworthy that in the quasistatic regime, the wettability of substrates plays an important role in determining the transfer ratio. Experimental results suggest that liquid will transfer to the more wettable surface at low Ca regime [54].

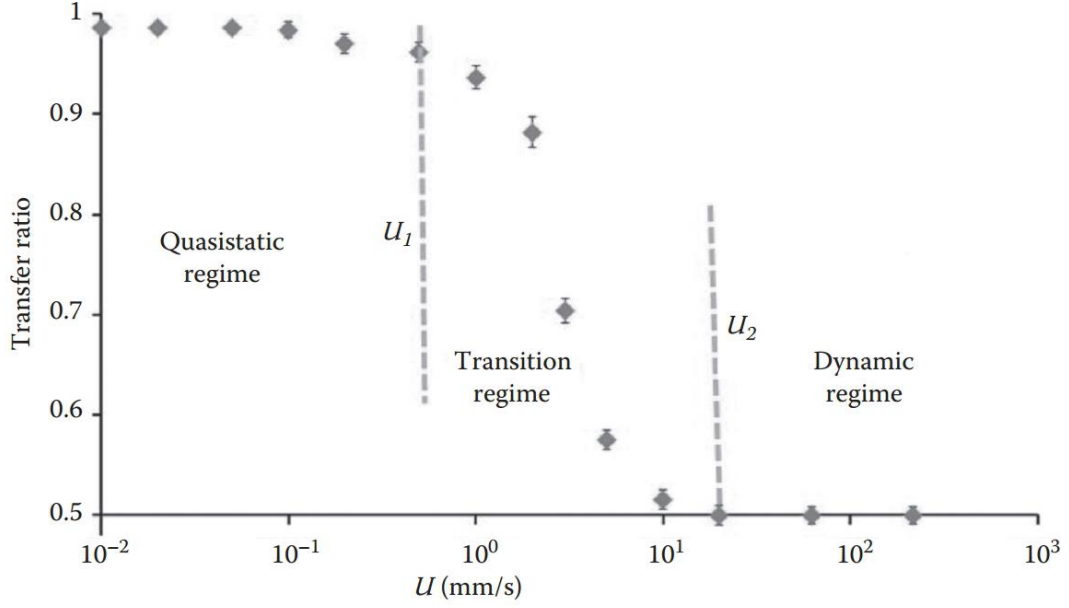


Fig. 2.9 Relation between transfer ratio, ω , and stretching speed U for glycerol transferred from OTS to PEMA surfaces, and three regimes are identified [57].

2.4 SPH methods for capillary interactions

In this section, the SPH method is briefly introduced with emphasis on reviewing existing approaches for surface tension and dynamic contact angle modelling. SPH method is a fully mesh-free, Lagrangian particle numerical method proposed and developed by Gingold and Monaghan [58] and Lucy [59] in 1977. One of the major topics studied in SPH is interfacial flows including floating body simulation [60] and multiphase studies [61, 62]. Although one of the main challenges faced by SPH is the problem of size, this challenge can be overcome with the use of massively parallel implementations [63]. In SPH models, the fluid is represented by a discrete set of N particles. The position of the i^{th} particles is denoted by the vector, \mathbf{r}_i , $i = 1, \dots, N$. SPH theory is based on the idea that continuous variables are represented as the superposition of smoothing functions centred on a set of discrete particle points, \mathbf{r}_i , as shown in Fig. 2.10. Detailed SPH formulations and discretisation of Navier-Stokes (N-S) equations will be described in Chapter 3.

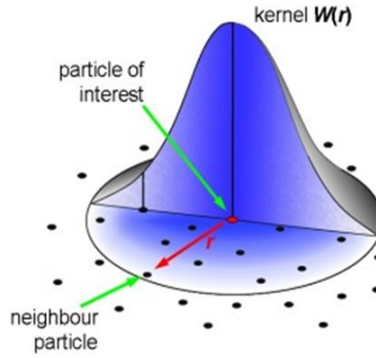


Fig. 2.10 Particle approximation in SPH method.

2.4.1 Advantages and disadvantages of SPH methods

A good knowledge of advantages of SPH method is helpful in deciding whether SPH is suitable for a particular problem. A few notable points from academic reviews [64, 65] that introduce the relative advantages of SPH are listed below:

- a) Compared with grid based methods, it is easier to vary spatial and temporal resolution in SPH. In grid based methods, sophisticated schemes are required in order to change grid size and indexing [66]. While, in SPH the smoothing length can be adjusted according to relatively simple criteria.
- b) It is also easy to include additional physics and transport equations in SPH which makes numerical computations to be explicit. Another advantage lies in the increased accuracy, the Lagrangian form treat fluid displacement in an intrinsic manner instead of an iterative procedure. This leads to reduced effects of numerical diffusion on velocity and momentum.
- c) Due to the Lagrangian particle nature of SPH, explicit interface tracking or capturing is not required. The difficulties associated with grid-based continuum numerical methods to processes with complex dynamic interfaces and/or boundaries is avoided.

Therefore, SPH is an ideal choice for modelling free surface and interfacial flow problems.

It is also necessary to keep in mind the following disadvantages of SPH:

- a) Numerical issues such as tensile instability [67] sometimes limit the range of problems can be addressed. In fluid dynamics problems, tensile instability can be resolved by applying sufficiently large positive background pressure to avoid the formation of negative pressure regions. In the literature, adding artificial pressure [68], higher order kernels [69] and kernel gradient correction [70] can handle the tensile instability issue.

- b) Compared with grid-based methods which can be designed to suit a particular problem by defining and modifying mesh geometry [71], SPH sometimes can lead larger errors because the Lagrangian nature of SPH makes it more difficult to control particle parameters, for instance, to allow changes of particles in size and number.
- c) Computational resource requirements can often be significantly greater for SPH method than their grid-based counterparts. Steady state solutions for many fluid dynamics problems are more time-consuming with SPH than finite elements due to the time-step restrictions for stable solutions of good quality [72].

2.4.2 Implementation of surface tension in SPH

Traditional SPH methods impose zero pressure Dirichlet boundary condition to free surface particles and thus make it difficult to implement a surface tension model at the free surface. However, a reliable surface tension model is required for numerical simulation of dynamic capillary interactions. In SPH, multiphase flow with surface tension have been modelled with different methods described as follows.

Brackbill et al. [73] proposed Continuum Surface Force (CSF) method to model surface tension effects where the surface force per unit mass is approximated by:

$$F_s = \frac{\sigma \kappa \mathbf{n} \delta(s)}{\rho}, \quad (2.11)$$

where σ is the surface-tension coefficient, $\kappa = -\nabla \cdot \mathbf{n}$ is the average curvature, \mathbf{n} is the unit outward normal, and $\delta(s)$ is a one-dimensional delta function of the distance s perpendicular to the surface. This method consists of identifying the normal to the target surface by assigning a colour C to each fluid particle and finding the gradient of the colour function from $\mathbf{n} = \nabla C / |\nabla C|$, e.g., $\nabla C = \sum_b \frac{m_b(C_b - C_a)}{\rho_b} \nabla_a w_{ab}(h)$. The curvature can then be calculated by an SPH form of the divergence of \mathbf{n} .

Yeganehdoust et al. [74] developed an efficient CSF method to track and correct colour function of boundary particles. The static contact angles, liquid droplet evolution and dynamic wetting angles on inclined surfaces and droplets collision have been successfully reproduced. Hu & Adams [61] modified the particle smoothing function for pressure and gradient terms and an alternative form of the colour gradient function is applied, in which the steady equilibrium droplets, capillary waves and drop deformations in shear flow have been achieved [75].

Another approach is to treat the SPH particles as real physical particles and superimpose forces in between to create the effects of surface tension [76, 77], i.e., Inter-Particle Force (IPF) model. For example, Tartakovsky and Meakin [76] implemented pairwise particle-particle interactions with the following force/mass between particles separated by a distance r :

$$F(r_{ij}) = \begin{cases} s_{ij} \cos\left(\frac{3\pi}{2h}\right) r_{ij}, & r_{ij} \leq h \\ 0, & r_{ij} > h \end{cases}. \quad (2.12)$$

The force $F(r_{ij})$ is repulsive for r_{ij} less than $h/3$, attractive for r_{ij} between $h/3$ and h , and zero for r_{ij} larger than h . The choice of parameter s_{ij} depends on the properties of different fluids and it is expected to be proportional to the surface tension. This surface-tension model is applied onto a series of problems involving drops, and fluid moving through fractures, and satisfactory results have been obtained.

2.4.3 Prescribing dynamic contact angle in SPH

The numerical simulation of capillary interactions in multiphase flow requires appropriate liquid-solid interactions and boundary conditions for reproducing dynamic contact angle. In the literature, there are only a few approaches are developed for prescribing dynamic contact angle in SPH. Tartakovsky and Panchenko [21] applied the dynamic Young–Laplace boundary condition at the fluid–fluid interface to obtain the rate-dependent contact angle at triple-line region. Huber et al. [12] introduced a Contact Line Force (CLF) model where the interfacial tension tangential to the solid interface is balanced by a driving force acting on the contact line, so the dynamic contact angle and moving contact line is properly implemented. Hochstetter and Kolb [78] directly applied the Cox’s law [8] to reproduce the dynamic contact angle, which is related to the third power of Ca . In addition, Farrokhpanah [79] applied dynamic contact angle by correcting the unbalanced force in the colour function near the contact line. However, the aforementioned approaches either lack direct links to realistic physical quantities that usually involved in complex flow conditions, or require explicit modelling of all phases in the pore space thus the computational cost is dramatically increased. Therefore, a new approach for tackling dynamic contact angle in SPH method will be desired in Chapter 3.

Chapter 3

SPH Method and Numerical Model

The SPH method is a fully mesh-free, Lagrangian method proposed by Gingold and Monaghan [58] and Lucy [59] independently for astrophysical problems. With the continuous development of the method, SPH is capable of handling many categories of engineering and physics problems. By imposing interpolation on the smoothing kernel, it is possible to estimate the derivatives of particle properties including pressure, density and viscosity. Gravitational forces can be implemented by summing over the particles with prescribed algorithms. In this chapter, the SPH method and selection of smoothing function are introduced, followed by the SPH discretisation of N-S equation, implementation of particle-particle interaction force model, and the newly-introduced interfacial viscous force formulation for accounting the dynamic capillary interactions.

3.1 SPH method

3.1.1 Smoothing function

The SPH method is based on the idea that a continuous field $A(\mathbf{r}_i)$ at position \mathbf{r}_i can be smoothed by a convolution integral with smoothing function, $W(\mathbf{r}_i - \mathbf{r}_j, h)$, allowing the value of any function to be obtained at a given point with neighbouring particles:

$$A(\mathbf{r}) = \int_{\Omega} A(\mathbf{r}') W(\mathbf{r} - \mathbf{r}', h) d\mathbf{r}', \quad (3.1)$$

where h is smoothing length. The correctness for the approximation Eq. (3.1) should be ensured by imposing several conditions on the smoothing function. The first is the normalization condition, which requires the integral of the smoothing function equal to 1:

$$\int_{\Omega} W(\mathbf{r} - \mathbf{r}', h) d\mathbf{r}' = 1. \quad (3.2)$$

The second condition is the delta-function property, where W should become a Dirac delta function in the $h \rightarrow 0$ limit [80]:

$$W(\mathbf{r} - \mathbf{r}', h) \xrightarrow{h \rightarrow 0} \delta(\mathbf{r} - \mathbf{r}') . \quad (3.3)$$

The integral of Eq. (3.1) is cast in the discrete form for computational use:

$$A(\mathbf{r}_i) = \sum_j A(\mathbf{r}_j) \frac{m_j}{\rho_j} W(\mathbf{r}_i - \mathbf{r}_j, h), \quad (3.4)$$

where m_j and ρ_j are mass and density of the j^{th} particle, respectively.

3.1.2 Approximation of the function's gradient

Following Monaghan [65], the approximation of function gradient $\nabla A(\mathbf{r})$ is obtained by the gradient of the smoothing function:

$$\nabla A(\mathbf{r}) = \int_{\Omega} A(\mathbf{r}') \nabla W(\mathbf{r} - \mathbf{r}', h) d\mathbf{r}', \quad (3.5)$$

where $\nabla W(\mathbf{r} - \mathbf{r}', h)$ is the gradient of the smoothing function. In the discrete form, Eq. (3.5) is rewritten as:

$$\nabla A(\mathbf{r}_i) = \sum_{j=1}^n \frac{m_j}{\rho_j} A(\mathbf{r}_j) \nabla W(\mathbf{r}_i - \mathbf{r}_j, h). \quad (3.6)$$

In general, the summation in Eq. (3.6) is conducted over all particles in the computational domain. When a smoothing function with compact support domains are imposed, the summation is only applied to the neighbouring particles within the range of smoothing length.

3.1.3 Forms of smoothing functions

A variety forms of smoothing functions have been used in SPH models, including Gaussian kernel [58], quadratic kernel [81], cubic-spline kernel [82], and fourth-order kernel [83]. Generally, the accuracy of the SPH interpolation increases with the order of the polynomial used in the smoothing function (except for the Gaussian kernel which has an exponential form). However, the computational time also increases with the order of the kernels. In this study, a Gaussian kernel is adopted for the proposed SPH model considering both calculation accuracy and computational efficiency:

$$W(\mathbf{r}, h) = \frac{1}{h\sqrt{\pi}} e^{-\left(\frac{r^2}{h^2}\right)}. \quad (3.7)$$

3.2 Numerical model

The Lagrangian form of Navier-Stokes equation for an incompressible Newtonian fluid is expressed as follows:

$$\frac{d\mathbf{v}_i}{dt} = -\frac{\nabla P}{\rho_i} + \mu \frac{\nabla^2 \mathbf{v}_i}{\rho_i} + \mathbf{F}, \quad (3.8)$$

where \mathbf{v}_i is flow velocity, P is pressure, ρ is density, $\mu \frac{\nabla^2 \mathbf{v}_i}{\rho_i}$ is the viscous term, and \mathbf{F} corresponds to the total volumetric force acting on unit mass. To represent the conservation of the mass for fluid flow, the continuity equation is usually written in the following form:

$$\frac{d\rho}{dt} = -\rho \nabla \cdot \mathbf{v}_i. \quad (3.9)$$

Using the definitions of gradients derived above, the Navier-Stokes Eq. (3.8) and (3.9) can be written in SPH form now.

3.2.1 Momentum equation

The approximation of function gradient in Eq. (3.6) can be applied to the pressure gradient term in Eq. (3.8) to have:

$$\nabla P_i = \sum_j \frac{m_j}{\rho_j} P_j \nabla_i W(\mathbf{r}_i - \mathbf{r}_j, h), \quad (3.10)$$

This approximation of Eq. (3.10) has the advantage that local pressure gradient becomes zero-valued when the spatially pressure field is constant [84]. However, Eq. (3.10) does not guarantee the conservation of linear or angular momentum and it is difficult to construct a consistent energy equation. Therefore, the pressure gradient should be symmetrised by rewriting $\nabla P/\rho$ to ensure momentum conservation [65]:

$$\frac{\nabla P_i}{\rho_i} = \nabla \left(\frac{P}{\rho} \right)_i + \frac{P_i}{\rho_i^2} \nabla \rho_i. \quad (3.11)$$

By applying approximation of Eq. (3.6), the following equation for the pressure gradient is obtained:

$$\nabla P_i = \rho_i \sum_j m_j \left[\frac{P_i}{\rho_i^2} + \frac{P_j}{\rho_j^2} \right] \nabla W(\mathbf{r}_i - \mathbf{r}_j, h), \quad (3.12)$$

and the momentum equation becomes:

$$\frac{d\mathbf{v}_i}{dt} = - \sum_j m_j \left[\frac{P_i}{\rho_i^2} + \frac{P_j}{\rho_j^2} \right] \nabla W(\mathbf{r}_i - \mathbf{r}_j, h) + \mu \frac{\nabla^2 \mathbf{v}_i}{\rho_i} + \mathbf{F}. \quad (3.13)$$

The viscous term is subjected to modification which will be discussed later in Section 3.3.4. For gravitational flows, the term \mathbf{F} can be substituted by the vector \mathbf{g} to represent gravity. Additional external forces, e.g., liquid-solid particle interactions, can be added to the last term in Eq. (3.13) for different scenarios.

3.2.2 Continuity equation

The continuity equation for particle i can be written directly with the approximation of Eq. (3.5):

$$\rho_i = \sum_j m_j W(\mathbf{r}_i - \mathbf{r}_j, h). \quad (3.14)$$

In this approach, the density of a given particle is directly calculated based on the particle masses of its neighbouring points, which is simple and straightforward. However, Monaghan [65] pointed out that this approach would suffer several major disadvantages when simulating free surface flows. As a result, another approach for computing the density of particle is applied in this work to solve the continuity equation as

$$\frac{d\rho_i}{dt} = \sum_j m_j \mathbf{v}_{ij} \nabla W(\mathbf{r}_i - \mathbf{r}_j, h), \quad (3.15)$$

where $\mathbf{v}_{ij} = \mathbf{v}_i - \mathbf{v}_j$ is the relative velocity of the i^{th} particle with respect to j^{th} particle.

3.3.3 Equation of State (EOS)

Originally the SPH method was proposed to deal with astrophysical problems [58, 59], which can be handled by applying EOS for the ideal gas. In terms of fluid simulation, the real fluid can be treated as a weakly-compressible fluid, where the compressibility of simulated liquid is artificially controlled by different choices of constants in EOS. In this work, the Tait EOS [64] is applied to define the motion of particle:

$$P = \frac{c^2 \rho_0}{\varepsilon} \left[\left(\frac{\rho_i}{\rho_0} \right)^\varepsilon - 1 \right], \quad (3.16)$$

where c is artificial speed of sound, ρ_0 is reference density of fluid, and ε is a constant.

According to Morris [85], the artificial sound speed must be chosen carefully to ensure the efficiency and accuracy of SPH solutions. The artificial sound speed should be large enough to ensure the behaviour of the corresponding fluid is sufficiently close to the real fluid, while reasonably small to make the time step practical in the calculation. Adami et al. [86] suggested that the artificial sound speed should be chosen at least one order of magnitude larger than the maximum velocity of particles in order to limit the effect of compressibility on the flow. In this work, we choose the artificial speed of sound as $c = 10V_{max}$ along with $\varepsilon = 7$, where V_{max} is the expected maximum particle velocity during simulations.

3.3.4 Artificial viscosity

In this work, a Monaghan style artificial viscosity [65] is adopted in the proposed model, to model viscous effect, prevent strong shocks and stabilise the numerical algorithm. The artificial viscosity is obtained by writing the momentum equation with following form:

$$\mu \frac{\nabla^2 \mathbf{v}_i}{\rho_i} = - \sum_j m_j [\Pi_{ij}] \nabla W(\mathbf{r}_i - \mathbf{r}_j, h), \quad (3.17)$$

where Π_{ab} is given by:

$$\Pi_{ij} = \begin{cases} \frac{-\alpha \bar{c}_{ij} \mu_{ij} + \beta \mu_{ij}^2}{\bar{\rho}_{ij}} & \mathbf{v}_{ij} \cdot \mathbf{r}_{ij} < 0 \\ 0 & \mathbf{v}_{ij} \cdot \mathbf{r}_{ij} > 0 \end{cases}, \quad (3.18)$$

and

$$\mu_{ij} = \frac{h \mathbf{v}_{ij} \cdot \mathbf{r}_{ij}}{\mathbf{r}_{ij}^2 + 0.01h^2}, \quad (3.19)$$

where α and β are constants, $\bar{c}_{ij} = (c_i + c_j)/2$ and $\bar{\rho}_{ij} = (\rho_i + \rho_j)/2$ refer to the values of the artificial sound speed and the density averaged between particles i and j , respectively. The viscosity vanishes when two particles move away from each other ($\mathbf{v}_{ij} \cdot \mathbf{r}_{ij} > 0$), Otherwise, when particles approach each other ($\mathbf{v}_{ij} \cdot \mathbf{r}_{ij} < 0$), the value of the viscous term is increased, thus stabilizing the numerical solution.

The term involving α are responsible for creating shear and bulk viscosity, while the term involving β is used to prevent unphysical penetration of particles that approach each other at a

high speed. Monaghan suggested the values for α and β are 1 and 2, respectively, for best results [65]. In this work, we adopt the α value while change the value of β to 0 as the motion of fluid flow in the simulation is relatively slow (ranging from 0.0002 to 20 mm/s). It should be noted that the implementation of this artificial viscosity could lead to unphysically high shear viscous forces because SPH simulations are stabilized by a fluid's physical viscosity, and it is challenging to simulate low viscous flows [87]. Therefore, our simulations will be carried out with this high viscous setting, and the apparent viscosity will be calibrated later in Section 4.2.

3.3.5 XSPH correction

An equation of motion called XSPH formulation is added to the momentum equation, continuity equation, and equation of state to close the system of governing equations [65, 88]:

$$\frac{d\mathbf{r}_i}{dt} = \mathbf{v}_i + \psi \sum_j m_j \frac{2(\mathbf{v}_i - \mathbf{v}_j)}{\rho_i + \rho_j} W(\mathbf{r}_i - \mathbf{r}_j, h), \quad (3.20)$$

where ψ is constant between 0 and 1. Using this XSPH correction in the equation of motion helps to move particles with average velocity, thus more consistent for the algorithm. This can potentially reduce the noise induced by pressure gradients, thus stabilising the free surface of liquid, and prevent the unphysical penetration of particles passing through each other.

3.3.6 Time integration

The choice of time step Δt is important in terms of balancing simulation stability and computational cost. Due to the explicit nature of the time stepping scheme, Δt must be smaller than certain values in order to stabilize the simulation. On the other hand, smaller Δt will cost more computational resource for simulation. For the weakly-compressible SPH formulation, the time step Δt must satisfy (1) the CFL-condition based on the maximum artificial sound speed and the maximum flow speed [85]:

$$\Delta t \leq 0.25 \frac{h}{c_{max} + |u_{max}|}, \quad (3.21)$$

(2) the magnitude of particle acceleration f_i

$$\Delta t \leq 0.25 \min_i \sqrt{\frac{h}{f_i}}, \quad (3.22)$$

and (3) the viscous condition

$$\Delta t \leq 0.125 \frac{h^2}{\mu}. \quad (3.23)$$

3.3 Inter-particle force model in SPH

Implementation of the surface tension effects into SPH model has been a challenging task. As discussed in the Chapter 2, there are two typical models for generating surface tension effects in the SPH method, Continuum Surface Force (CSF) model and Inter-Particle Force (IPF) model. Compared with the CSF model, the IPF model demonstrates some advantages. Firstly, the algorithm of IPF model is simpler because it does not require the calculation for normal vector and curvature of the interface. In addition, the interactions between different phases can be easily generalized with IPF model, resulting well-defined contact angles under both static and dynamic conditions.

In this work, an inter-particle force formulation proposed by Li et al. [89] is applied to reproduce the surface tension and wetting effects. The pair potential energy $U(r)$ and inter-particle force \mathbf{F}_{ij}^{inter} are given as:

$$U(r) = \alpha_{ij} [CW^e(r, h_i) - DW^e(r, h_j)], \text{ where } h_i, h_j \leq 0.5h, \quad (3.24)$$

$$\mathbf{F}_{ij}^{inter} = -\frac{dU(r)}{dr} \frac{\mathbf{r}_i - \mathbf{r}_j}{\|\mathbf{r}_i - \mathbf{r}_j\|}, i \neq j, \quad (3.25)$$

where α_{ij} is inter-particle force strength parameter, C and D are constants, and W^e is the cubic spline function to construct the potential energy function with the form of:

$$W^e(r, h) \begin{cases} 1 - \frac{3}{2} \left(\frac{r}{h}\right)^2 + \frac{3}{4} \left(\frac{r}{h}\right)^3 & 0 < \frac{r}{h} \leq 1 \\ \frac{1}{4} \left(2 - \frac{r}{h}\right)^3 & 1 < \frac{r}{h} \leq 2 \\ 0 & \text{otherwise} \end{cases} \quad (3.26)$$

This smoothing function is normalized by $\frac{2}{3h}$, $\frac{10}{7\pi h^2}$, $\frac{1}{\pi h^3}$ in 1D, 2D and 3D space, respectively.

The inter-particle force in Eq. (3.25) is imposed on both liquid and solid particles to generate multiphase interactions between different phases. The parameter α_{ij} is set to α_1 when particle j is a liquid particle and set to α_2 when particle j is a solid particle. Note that particle i in Eq. (3.25) is always a liquid particle. By assigning different value for α_1 and α_2 , different surface

tension of free surface and static contact angle can be reproduced in the simulation. Moreover, to prevent the unphysically penetration of liquid particles into the solid particles, additional repulsive boundary forces are implemented similar to those implemented in Monaghan and Kajtar [90].

3.4 Interfacial viscous force formulation

In most SPH simulations, the boundaries of rigid bodies have been prescribed with different mechanisms, such as ghost particles [91], normalising conditions [92], and boundary particle forces [90], all of which are only appropriate for perfectly smooth boundaries [93]. In this work, considering the particle-particle interaction force at liquid-solid interface, the summation of the short range repulsive and longer range attractive forces acting on the liquid particle is zero on the tangential direction, which makes the interface also frictionless, see Fig. 3.1 (b). Therefore, the rate-dependent behaviour of moving contact line is hardly achieved in this circumstance.

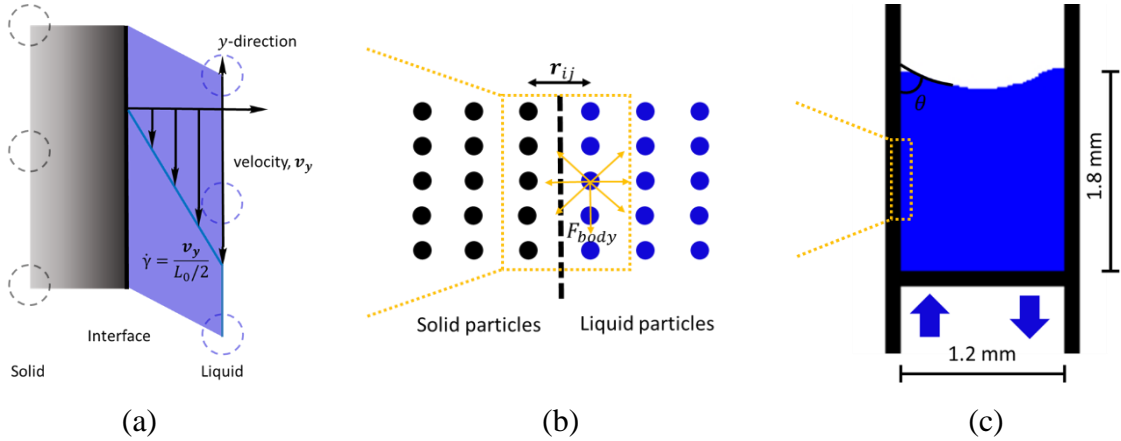


Fig. 3.1 Schematics of the modified SPH approach (not to scale): (a) Shearing between solid and liquid particles at the liquid-solid interface; (b) Force balance of a liquid particle; (c) Geometry of capillary tube for dynamic contact angle simulation.

There are several approaches in SPH to prescribe dynamic contact angle at the contact line, e.g., using Young–Laplace boundary condition at the fluid–fluid interface [21], and introducing a contact line force model [12]. However, the above approaches require explicit modelling of geometries and boundaries of all phases in the pore space thus the computational cost is dramatically increased. In this work, we introduce a new algorithm which imposes a viscous force \mathbf{F}_i^{vis} on the liquid particles at liquid-solid interface to reproduce the rate-dependent behaviour of moving contact line:

$$\mathbf{F}_i^{vis} = -S \cdot \tau = -L_0 \cdot \eta \cdot \dot{\gamma} = -L_0 \cdot \eta \cdot \frac{\mathbf{v}_i - \mathbf{v}_j}{L_0/2} \quad (3.27)$$

where S is liquid-solid contact area, and in two-dimensional case the contact area becomes the particle spacing L_0 , τ is shear stress, η is the viscosity of bulk fluid, $\dot{\gamma}$ is shear rate, and $\mathbf{v}_i - \mathbf{v}_j$ is the relative velocity between liquid and solid particles. The thickness of shearing equals to half of the interface spacing L_0 considering the contact line is in the middle of solid-liquid interface, as shown in Fig. 3.1 (a). This formulation is based on assumptions of the laminar flow with a constant shear rate and no-slip boundary condition at the liquid-solid interface.

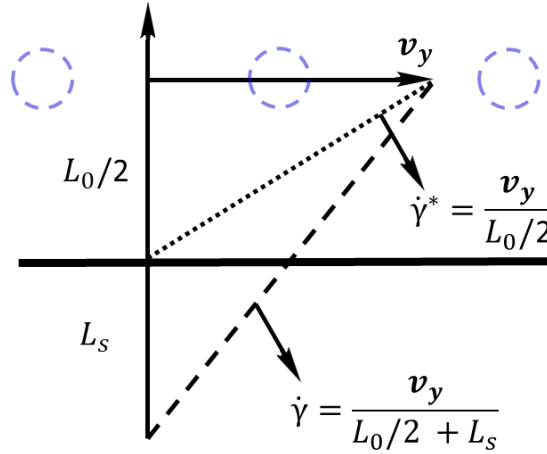


Fig. 3.2 Comparison between velocity profiles under the slip boundary (dashed line) and the equivalent model (dotted line).

To take the presence of the slip length into account, the interfacial force formulation in Eq. (3.27) needs to be modified. Fig. 3.2 illustrates the equivalent model for effective shear rate $\dot{\gamma}^*$ considering the slip boundary condition with a slip length of L_s . The equivalent model should have the same tangential force with the actual case with a slip condition, as:

$$\mathbf{F}_i^{vis} = -L_0 \cdot \eta^* \cdot \frac{\mathbf{v}_y}{L_0/2} = -L_0 \cdot \eta \cdot \frac{\mathbf{v}_y}{L_0/2 + L_s}, \quad (3.28)$$

where η^* is the equivalent viscosity at the interface. Thus, we have:

$$\eta^* = \eta \cdot \frac{L_0}{L_0 + 2L_s}. \quad (3.29)$$

Therefore, the bulk viscosity η at interface is replaced by a smaller value η^* ($L_s > 0$) to reproduce the actual shear profile at the liquid-solid interface. Finally, we have interfacial viscous force \mathbf{F}_i^{vis} added in the inter-particle force formulation with the following form:

$$\mathbf{F}_i^{vis} = \begin{cases} -L_0 \cdot \eta^* \cdot \frac{\mathbf{v}_i - \mathbf{v}_j}{L_0/2}, & r_{ij} \leq L_0 \\ 0 & , r_{ij} > L_0 \end{cases}. \quad (3.30)$$

This formula also includes the mesh size, L_0 , and mesh sensitive studies have been conducted to verify Eq. (3.30). Modified with the inter-particle interaction force, \mathbf{F}_{ij}^{inter} , and interfacial viscous force, \mathbf{F}_i^{vis} , the SPH discretisation of the governing equations now can be read as follows:

$$\frac{d\mathbf{v}_i}{dt} = - \sum_j m_j \left[\frac{P_i}{\rho_i^2} + \frac{P_j}{\rho_j^2} + \Pi_{ab} \right] \nabla W(\mathbf{r}_i - \mathbf{r}_j, h) + \mathbf{g} + \sum_j \frac{\mathbf{F}_{ij}^{inter}}{m_i} + \frac{\mathbf{F}_i^{vis}}{m_i}. \quad (3.31)$$

The parameters used in this work is listed in Table 3.1. unless otherwise mentioned. This SPH model is implemented in an open source framework PySPH [94].

Table 3.1. Parameters for dynamic contact angle simulations.

Parameters	Symbols	Value
Density (kg/m ³)	ρ_0	1000.0
Gravity (m/s ²)	g	9.8
Viscosity (Pa·s) [^]	η	0.013, 0.04, 0.185
Interfacial viscosity (Pa·s)	η^*	0 ~ 0.009
Surface tension (N/m) [^]	γ	0.28
Particle mass (kg)	m_0	6.25×10^{-7}
Particle spacing (m)	L_0	2.5×10^{-5}
Smoothing length (m) [†]	h	7.5×10^{-5} ($=3L_0$)
Artificial sound speed (m/s)	c	3.0
Time step (s)	Δt	4.15×10^{-7}
Liquid-liquid interaction force parameter (J)	α_1	5.42×10^{-4}
Liquid-solid interaction force parameter (J)	α_2	5.69×10^{-4}

[^]These material properties are the results of other input parameters.

[†]Sufficient particles should be contained in a smoothing area to get a smoother result. Unnatural stiffness of fluid particles occurred in the simulation tests with smoothing length smaller than

$2L_0$ due to a lack of neighbouring particles. Hence, $h = 3L_0$ was used in this work considering both simulation accuracy and computational efficiency.

Chapter 4

Identification of Model Parameters

In this chapter, we firstly present the density and pressure profile of a stable state droplet, and the viscosity of the simulated fluid is derived from Poiseuille's Law. The inter-particle force formulation is validated by simulating the shape evolution of droplet in vacuum, and surface tension is calibrated afterwards. Subsequently, static contact angles with different liquid-solid inter-particle force parameters are reproduced to evaluate the performance of the multiphase interaction algorithm. Finally, the boundary condition is examined with gravity-driven flow in a capillary tube.

4.1 Density and pressure

In this section, a droplet composed of 32400 particles is simulated, and the density and pressure profile of this stable state droplet is presented. Fig. 4.1 shows the average density profile in terms of droplet radius, which describes the change of the density from the centre to the surface of the droplet. The radius of the droplet is 1.5 mm and the density has a stable value of 1000 kg/m³ within the region where R is less than 1.2 mm. The averaged density over the whole droplet is also 1000 kg/m³. However, for the area between 1.2 mm and 1.5 mm, the density profile starts to fluctuate due to the boundary deficiency [80]. The boundary deficiency refers to the inaccuracy of interpolation when the support domain of a particle is incomplete. In this case, since the droplet is simulated in vacuum, the supporting domain of the particle near droplet surface is incomplete and the smoothing results are not accurate. Therefore, we will only consider the values in bulk stable region to represent the real density of the droplet.

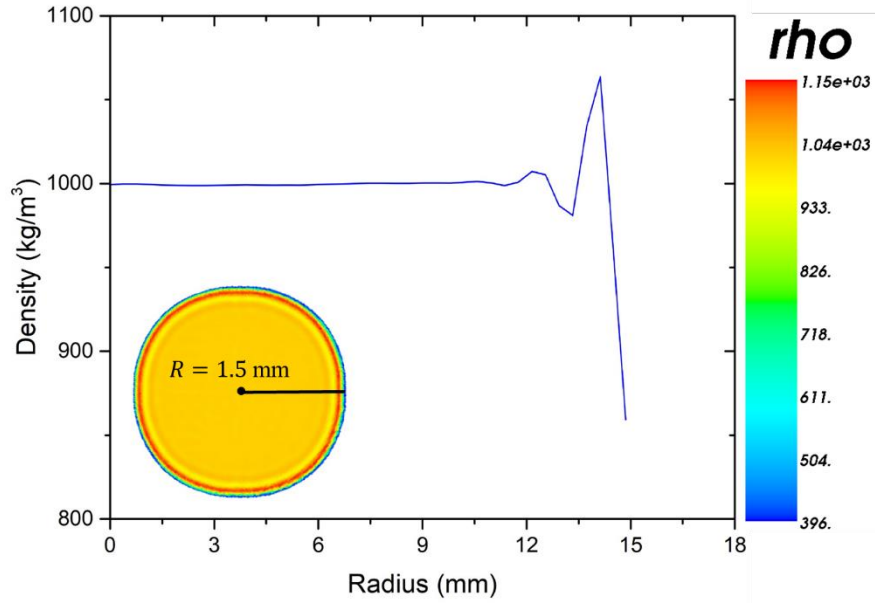


Fig. 4.1 Density profile of a steady state droplet.

The pressure profile of the stable state droplet is shown in Fig. 4.2. Similarly, the pressure at the edge of the droplet fluctuates a lot due to boundary deficiency. Again, we only took bulk stable pressure for droplet property calculation and calibration, such as surface tension and viscosity.

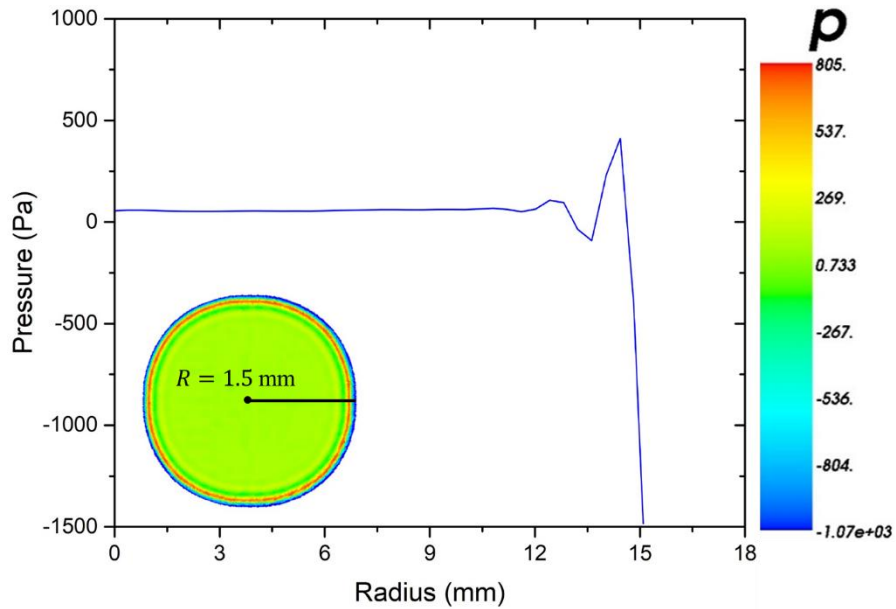


Fig. 4.2 Pressure profile of a steady state droplet.

It is noteworthy that the system should be in stable configuration for property calibration and calculation. For instance, the system potential energy evolution throughout the above calibration is shown in Fig. 4.3, which indicates the solution become stable after simulation

time $t=0.125$ s. Therefore, the values for pressure and density is taken after 0.125 s of simulation time.

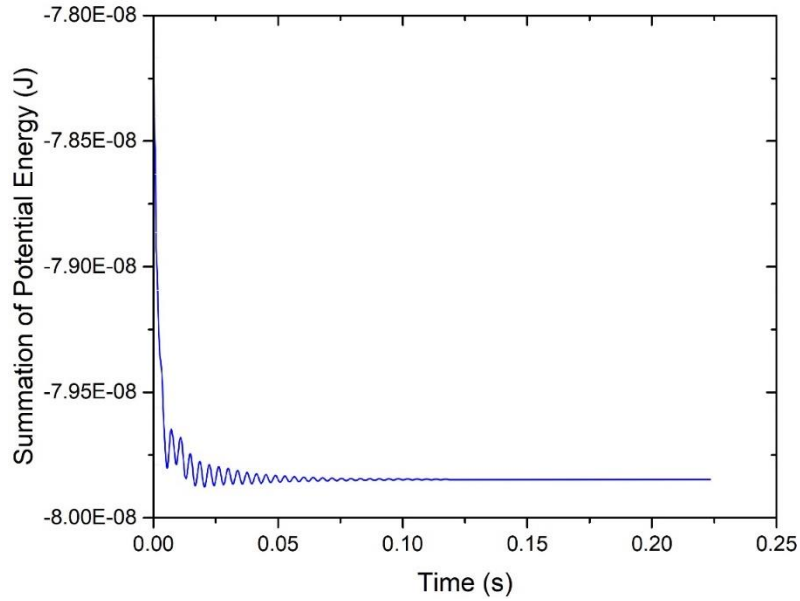


Fig. 4.3 Evolution of the system potential energy with respect to the simulation time.

4.2 Viscosity measurement

In addition to surface tension, viscosity is another principal parameter in fluid dynamics, and the accurate calculation of Ca relies on the value of fluid viscosity. In this work, the Hagen–Poiseuille equation [95] is applied to calculate the viscosity of the simulated fluid. The Hagen–Poiseuille equation describes the pressure drop of incompressible and Newtonian fluid flowing through a long cylindrical pipe, as shown in Fig. 4.4. In 3D case, the viscosity of fluid can be found in the following equation:

$$\Delta p = \frac{8\eta L Q}{\pi r^4}, \quad (4.1)$$

where Δp is the pressure reduction, L is the length of pipe, η is the dynamic viscosity, Q is the volumetric flow rate, r is the pipe radius.

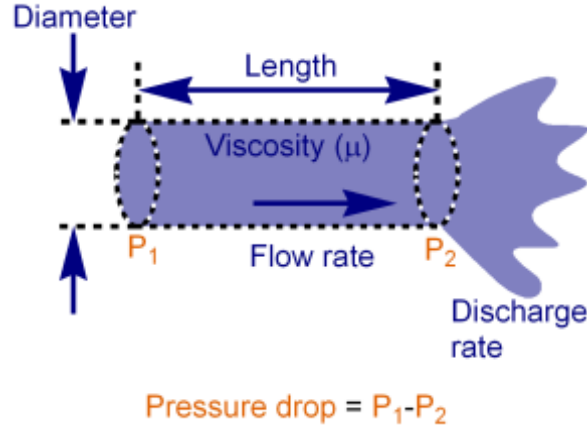


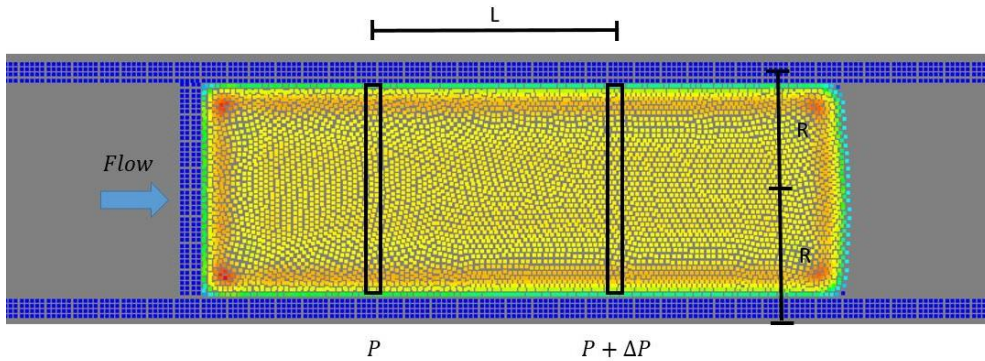
Fig. 4.4 Pressure drop for laminar flow in pipe [25].

While in 2D case, the equation turns out to be:

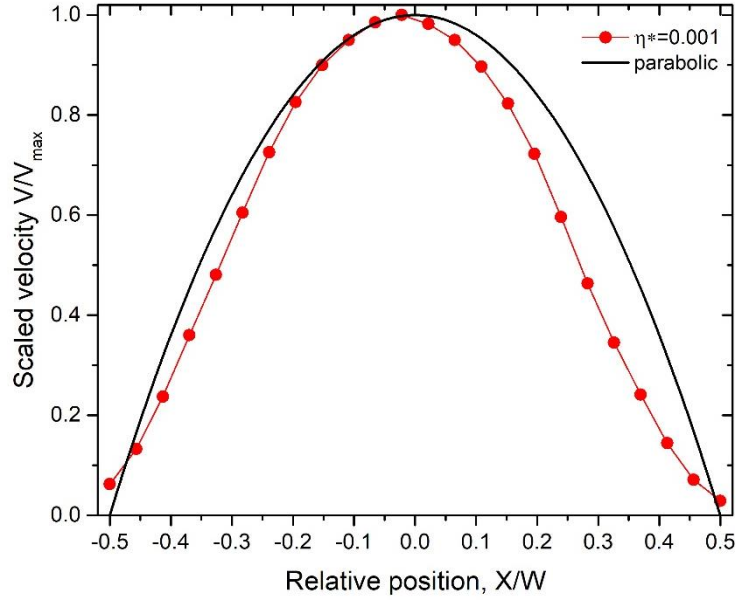
$$\Delta p = \frac{3\eta Lv}{r^2}, \quad (4.2)$$

where v is the velocity of flow. The derivation of 2D Hagen–Poiseuille equation is detailed in Appendix A.

A 2D Poiseuille flow as shown in Fig. 4.5 (a) is simulated to estimate the viscosity of fluid. The parameters for liquid and solid interactions are the same as those used for density and pressure calibration. The width of channel is 9 mm. The selected length of flow is $L = 16$ mm and this section is in the bulk region of pipe to avoid deviation due to boundary deficiency. A shifting boundary is driving the flow from left to generate a pressure difference. Then the pressure of two black blocks are measured and the pressure difference Δp is around 15 Pa. Finally, the calculated viscosity of this fluid is 0.04 Pa·s. In addition, the velocity profile of this Poiseuille flow as well as theoretical solution are plotted in Fig. 4.5 (b).



(a)



(b)

Fig. 4.5 (a) Simulation of pressure-driven Poiseuille flow for viscosity calculation; (b) Velocity profiles of steady Poiseuille flow and referenced parabolic plot.

4.3 Surface tension

To examine the surface tension scheme used in this study, the shape evolution of a 2D droplet with zero gravity in vacuum is presented. The simulation starts from a $2.6 \times 2.6 \text{ mm}^2$ square shape drop filled with liquid particles. Due to liquid-liquid interaction force which is short-range repulsive and longer range attractive, the fluid particles should eventually form a circular shape droplet to minimize the surface energy and surface area. The reference density of fluid for the simulation is set to 1000 kg/m^3 .

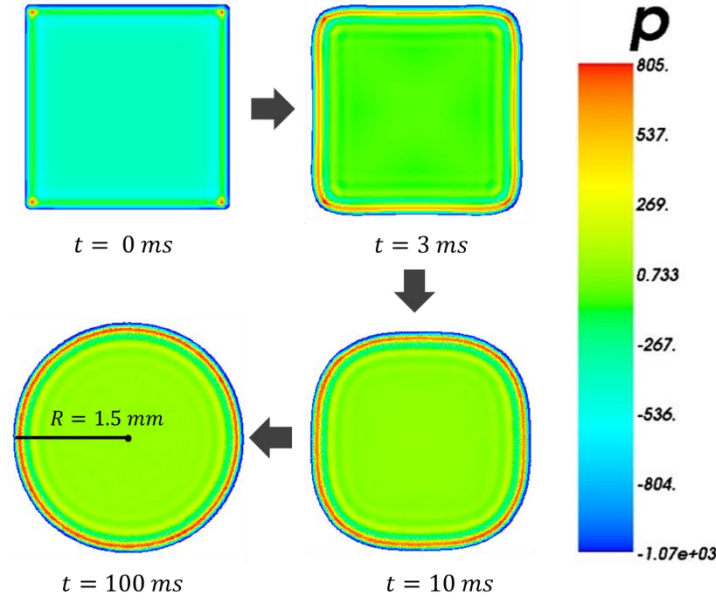


Fig. 4.6 Shape evolution of a droplet with zero-gravity in vacuum.

The shape evolution of the droplet is presented in Fig. 4.6. The droplet is square at simulation time zero, $t = 0$ ms. Due to the liquid-liquid interaction force, the surface of the droplet starts to evolve and finally turns into a circular shape at $t = 100$ ms.

The Young-Laplace equation in Chapter 2, Eq. (2.3) is used to calculate the surface tension, and in two-dimensional case, Eq. (2.3) becomes

$$\frac{\gamma}{R} = \Delta P. \quad (4.3)$$

Here ΔP is the averaged pressure of particles in the stable region, and R is measured from the outmost particle to the centre of the droplet. By altering the liquid-liquid inter-particle force parameter α_1 , this model can simulate different surface tension of free surface for various fluids. In this calibration, the total pressure of the droplet is the sum of pressure calculated from EOS plus the part generated by inter-particle force \mathbf{F}_{ij}^{inter} . Due to the boundary deficiency effect, we exclude the edge of droplet and use bulk region for pressure measurement. In Table 4.1, 7 different values of α_1 from 0.1×10^{-4} to 5.5×10^{-4} are tested and the resulted surface tension is calculated. It is observed that the surface tension of droplets increases linearly with α_1 , see in Fig 4.7. Therefore, we can tune the value of α_1 to get desired surface tension according the linear relationship.

Table 4.1. Summary of α_1 values and the corresponding surface tension

	low surface tension \rightarrow high surface tension							
α^{inter} (J)	0.1×10^{-4}	0.5×10^{-4}	1.0×10^{-4}	2.0×10^{-4}	3.0×10^{-4}	4.0×10^{-4}	5.0×10^{-4}	5.0×10^{-4}
Surface tension (γ)	0.0195	0.048	0.0795	0.147	0.21	0.2775	0.345	0.375

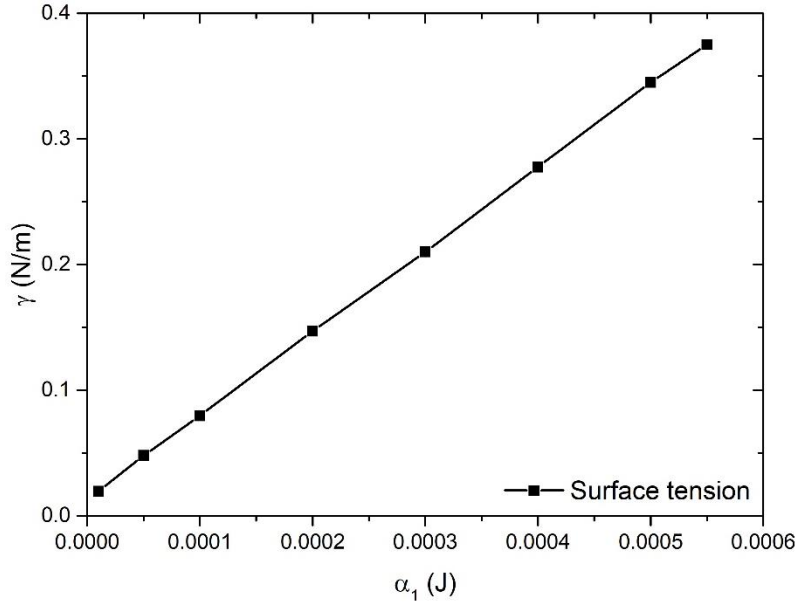


Fig. 4.7 Relationship between the α_1 and surface tension.

4.4 Contact angle

In this section, the contact angle calibration is conducted by simulating a droplet wetting solid surface with the liquid-solid interaction formulation. The liquid-liquid interaction parameter α_1 is set to 5.42×10^{-4} J, and a stable circular droplet is imported as the liquid phase for the initial configuration at $t = 0$ ms. The solid base is cut in rectangular shape with the dimension of $2.0 \text{ mm} \times 0.1 \text{ mm}$. The solid base particles are discretised to four layers in the y -direction, with a spacing of $2.5 \times 10^{-2} \text{ mm}$ and the bottom layer is fixed in the x - and y -directions.

Different wetting behaviour from hydrophobic to hydrophilic can be simulated by adjusting the liquid-solid interaction strength parameter α_2 , and six different equilibrium contact angles are simulated with α_2 ranging from 0 to 7.0×10^{-4} J. All the cases start from the same initial condition, and the droplet is slowly brought into contact with the flat surface under gravity. The simulation stops when the droplet configuration reaches a stable status. The final stable configurations of all cases are shown in Fig. 4.8, and the static contact angles are measured and listed in Table 4.2. The relationship between α_2 values and contact angles is plotted in Fig. 4.9 which indicates a monotonic correlation. This demonstrates that in this model, a desired static contact angle on a flat solid surface can be achieved by changing the α_2 value.

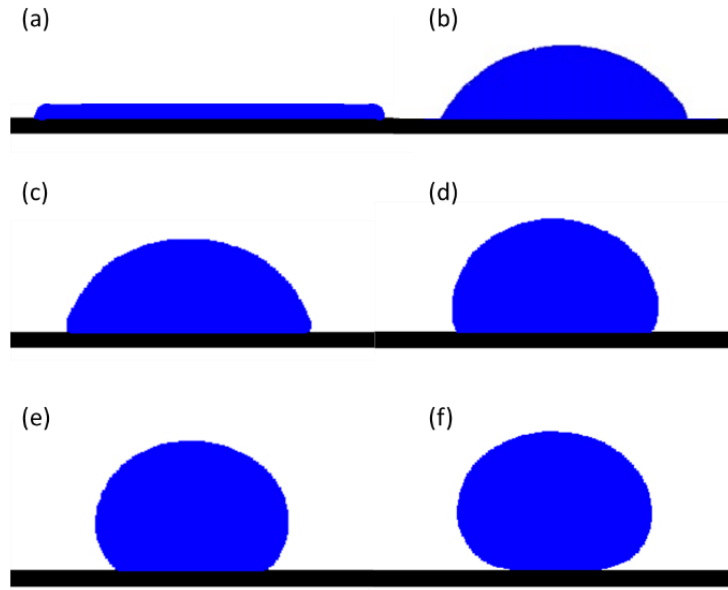


Fig. 4.8 Stable configurations of static contact angles on the solid surface.

Table 4.2. Summary of α_2 values and the corresponding contact angle

	hydrophilic \rightarrow hydrophobic					
α^{inter} (J)	6.92×10^{-4}	5.536×10^{-4}	4.607×10^{-4}	2.768×10^{-4}	1.384×10^{-4}	0
Contact angle ($^\circ$)	<10	45	75	105	135	>170
Figure	a	b	c	d	e	f

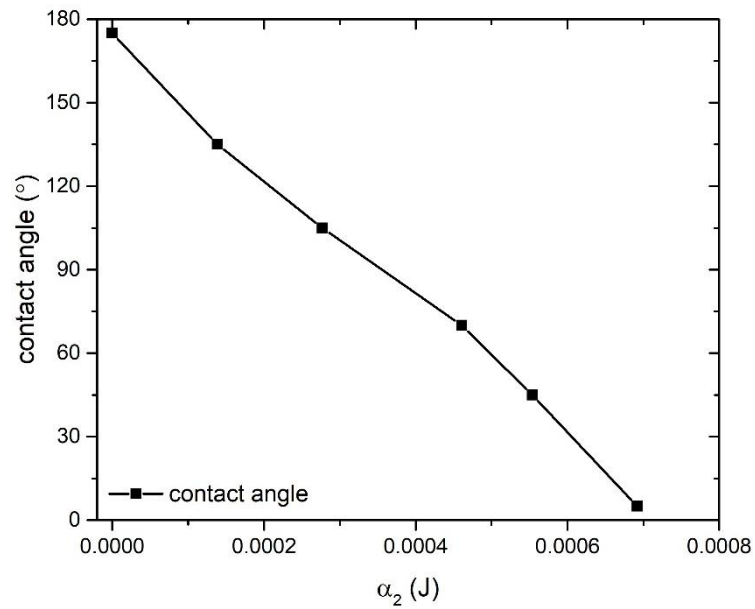


Fig. 4.9 Relationship between the α_2 and contact angle.

4.5 Boundary condition examination

The boundary condition is examined in this section. A gravity-driven flow is simulated as shown in Fig. 4.10. The fluid domain is 2 mm high and 1.2 mm wide with fixed solid boundary on the left and right sides. Periodical boundary condition is imposed on top and bottom of the fluid domain. The liquid-solid interaction strength parameter α_2 is set to 4.0×10^{-4} J with other parameters and constants same with the above-mentioned contact angle calibration.

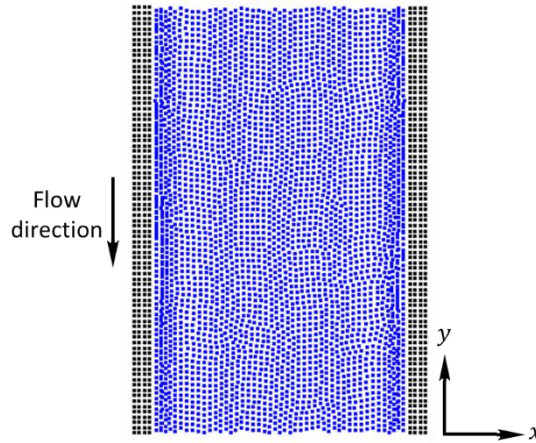


Fig. 4.10 Gravity-driven flow between two parallel plates.

The velocity profile in Fig. 4.11 is obtained by measuring and connecting the velocity along the flow cross section with more than 20 velocity points. The blue line refers to the velocity profile with interfacial viscous force implemented in the model, where the parameter η^* equals to 0.006 Pa·s. The red line represents the case without imposing interfacial viscous force formulation, and the black line is a parabolic plot of ideal velocity profile for no-slip condition. It can be observed that the velocity profile for both cases are quite close to the theoretical profile, which demonstrated the capability of proposed model in simulating different boundary condition, and the velocity of the liquid particles adjacent to the solid boundary is approaching zero. In principle, the no-slip boundary condition requires the velocity of the fluid adjacent to the boundary is zero, however in this case, the most left (or right) fluid particles can not fully represent the interface due to the existence of the space between solid and liquid particles. If the velocity is interpolated to the centre of the liquid-solid interface, the velocity would be almost zero. Therefore, this SPH model may possess various slip boundary conditions for different liquid-solid interface scenarios.

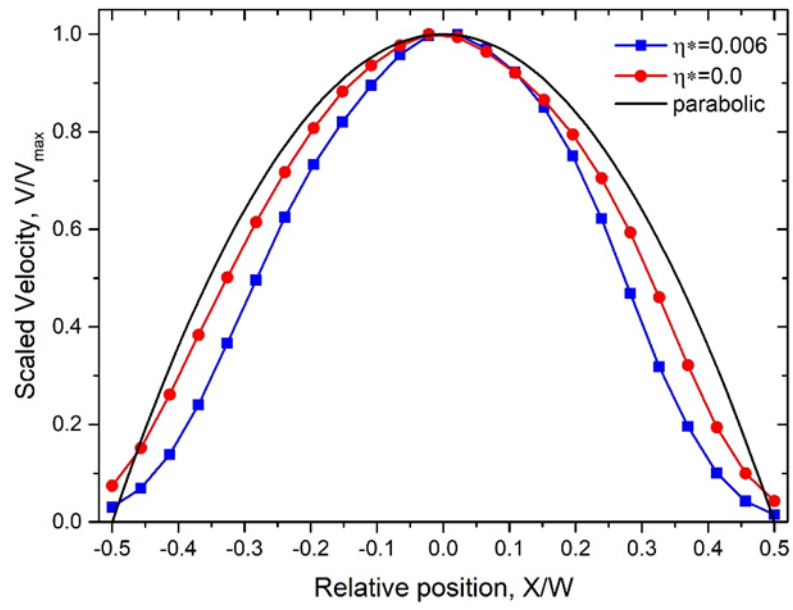


Fig. 4.11 Velocity profiles of steady gravity-driven flow and referenced parabolic plot.

Chapter 5

Dynamic Contact Angle

In this chapter, we will investigate the dynamic contact angle with the newly-introduced interfacial viscous force formulation. The parameters and geometry for the simulation is firstly introduced followed by the examination on the effectiveness of \mathbf{F}_i^{vis} . The simulated dynamic contact angle results are verified by the power law correlation mentioned in Chapter 2, and the influence of different magnitude of \mathbf{F}_i^{vis} on dynamic contact angle and power law fitting results is also studied. In addition, the viscosity ratio, $\frac{\eta^*}{\eta}$, is found to be responsible for achieving similar dynamic contact angle simulation results for fluids with different viscosity. Finally, the mesh sensitivity test and velocity field of capillary flow is conducted and discussed.

The content of this Chapter is based on the manuscript entitled ‘A Modified Smoothed Particle Hydrodynamics Approach for Modelling Dynamic Contact Angle Hysteresis’, Y. Bao, L. Li, L. Shen, C. Lei, and Y. Gan, 2018, in submission.

5.1 Simulation geometry and setup

To simulate the moving contact line and dynamic contact angle, a 2D capillary tube with a shifting substrate is modelled in vacuum with the following geometry and parameters. The size of the capillary tube is $4 \text{ mm} \times 1.36 \text{ mm}$ containing fluid with domain of $1.8 \text{ mm} \times 1.2 \text{ mm}$, as shown in Fig. 5.1. The characteristic length of the fluid is within capillary length l_c (2 mm), so the influence induced by gravity can be neglected as capillary and viscous force are dominating this system. Other parameters are listed in Chapter 3, and the value of interfacial viscous force parameter η^* will be stated in the following sections. The surface tension ($\gamma = 0.28 \text{ N/m}$) and bulk viscosity ($\eta = 0.04 \text{ Pa}\cdot\text{s}$) of the simulated fluid is fixed unless mentioned otherwise, and Ca is only controlled by the triple-line region velocity, v_t .

The contact angle θ is considered as the included angle by the tangent to the curvature of the fluid front and the vertical solid wall. The first three layers of liquid particles adjacent to the solid wall are neglected for curvature fitting, as these particles are frequently reconstructing

due to the liquid-solid interactions and boundary repulsive force, which results the triple-line region not suitable for a stable contact angle fitting.

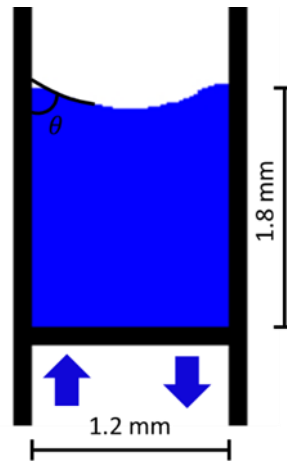


Fig. 5.1 Geometry of the capillary tube and contact angle determination.

The capillary tube is under same stable configuration before the bottom substrate starts moving. In all simulation cases, the bottom substrate moves along the y -direction for 1.2 mm to raise or withdraw the fluid with various velocities to generate a moving contact line. Fig. 5.2 shows snapshots of fluid movement and curvature at different simulation time. It can be observed in both advancing and receding cases, the initial configurations are the same in terms of fluid curvature and static contact angle. With the driving of the substrate, the fluid is either pushed up or lowered down depending on the direction of the substrate movement. The advancing angle occurs when the fluid is pushed up, and receding angle is formed when the substrate withdraws the fluid. For any given time step, the resulting contact angle will be recorded against the instantaneous contact line speed.

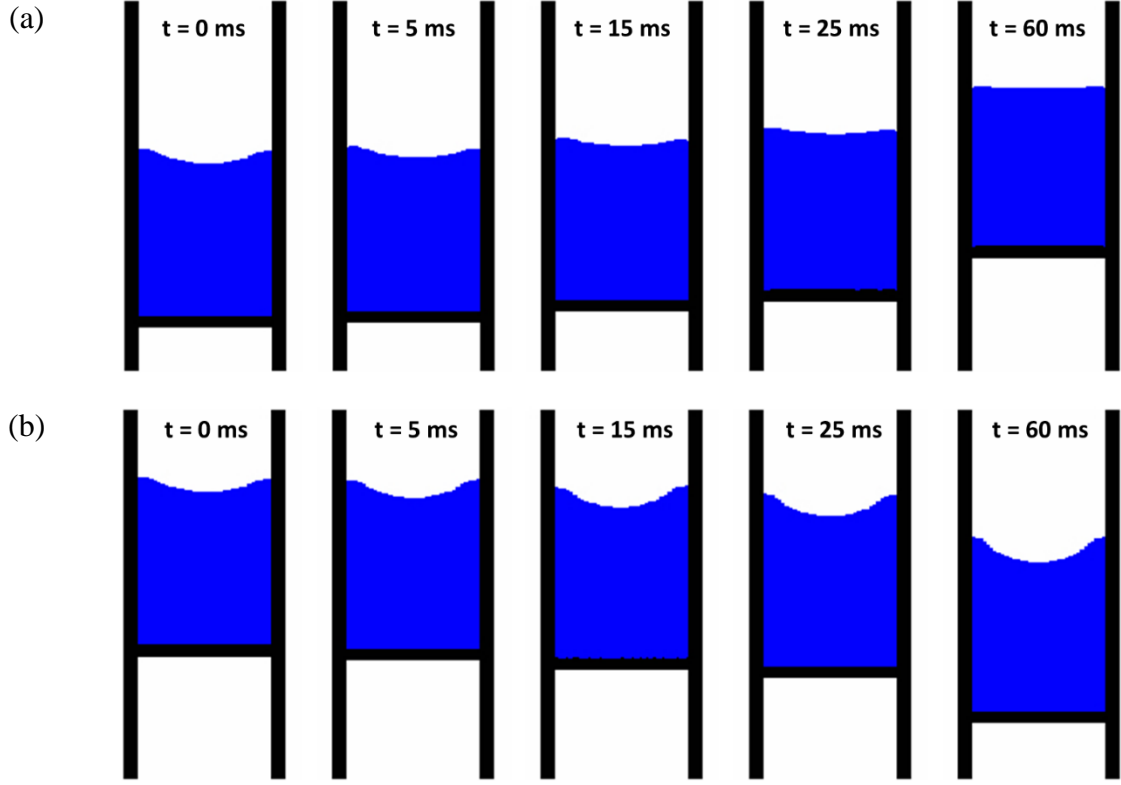


Fig. 5.2 Snapshots of dynamic contact angle simulation at various simulation time steps while the moving speed of substrate equals 10 mm/s: (a) advancing case; (b) receding case.

5.2 Effectiveness test for F_i^{vis}

In this section, the newly-introduced interfacial viscous force formulation is examined. For this purpose, we conducted two dynamic contact angle simulations, implemented with and without the interfacial viscous force F_i^{vis} , and the results are compared in terms of dynamic contact angle. The first case is implemented by the interfacial viscous force F_i^{vis} with parameter $\eta^* = 0.003$ Pa·s, and the other one does not consider the effect of F_i^{vis} where $\eta^* = 0.0$ Pa·s. Both cases are simulated with 12 sets of substrate moving speed ranging from 0.002 mm/s to 20 mm/s. The resulted Ca covers from 10^{-6} to 10^{-1} . Simulation results are plotted in scatters as shown in Fig. 5.3.

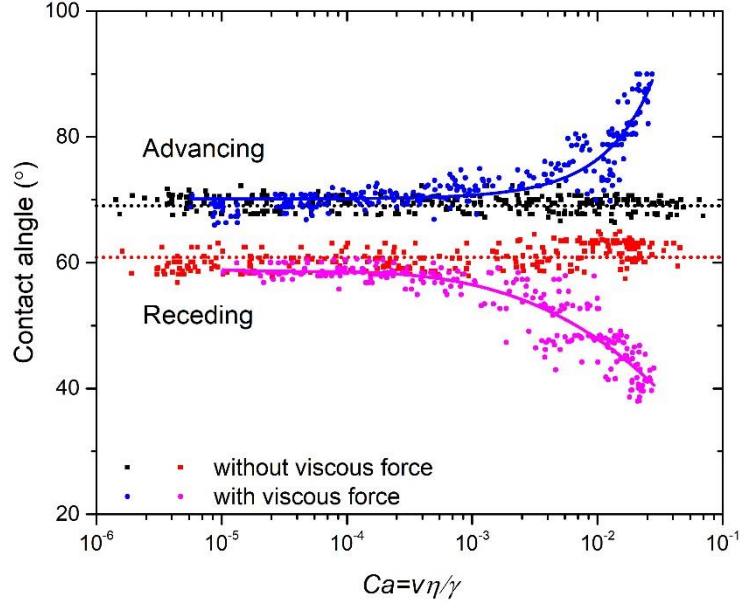


Fig. 5.3 Scattered plot of dynamic contact angle simulation with and without interfacial viscous force, \mathbf{F}_i^{vis} . Blue and pink circles: advancing and receding cases with \mathbf{F}_i^{vis} ; Black and red squares: advancing and receding cases without \mathbf{F}_i^{vis} .

For $Ca < 10^{-4}$, the dynamic contact angle simulation results are independent of \mathbf{F}_i^{vis} where the dynamic advancing/receding angle is around 70° and 60° , respectively. For $10^{-4} < Ca < 10^{-3}$, slight difference can be observed from the results. For cases implemented with \mathbf{F}_i^{vis} , the dynamic advancing angle starts to increase and the receding angle starts to decrease, while the dynamic contact angle without \mathbf{F}_i^{vis} remains unchanged. The major difference occurs in the large Ca regime ($Ca > 10^{-3}$): With the increase of Ca , the dynamic advancing/receding contact angle keeps almost constant in the case without \mathbf{F}_i^{vis} , which suggests there is no rate-dependent behaviour of dynamic contact angle. While for cases implemented \mathbf{F}_i^{vis} , the dynamic advancing angle increases from 70° to around 90° and the dynamic receding angle decreases from 60° to less than 40° .

The simulation results suggest that the interfacial viscous force formulation is the key for reproducing dynamic contact angle. According to Eq. (3.30) in Chapter 3, the interfacial viscous force \mathbf{F}_i^{vis} at liquid-solid interface region is increased with the velocity of liquid particles. Therefore, \mathbf{F}_i^{vis} will result in different influence on the motion of moving contact line depending on the magnitude of v_t . In the case where v_t is small ($Ca < 10^{-4}$), the magnitude of interfacial viscous force \mathbf{F}_i^{vis} is also neglectable, so the contact angle hysteresis is hardly observed within small Ca regime. When v_t becomes larger, \mathbf{F}_i^{vis} starts to influence

the behaviour of moving contact line. In such a circumstance, the relative motion of contact line is restricted and slowed down on the flow direction. Meanwhile, the bulk fluid in the middle region of capillary tube does not affected by the interfacial viscous force, so this part of fluid moves quicker than the fluid at triple-line region, which makes a larger (or smaller) contact angle for advancing (or receding) case. In summary, with the existence of this newly-introduced interfacial viscous force formulation, the SPH model can successfully simulate the dynamic contact angle.

Although the proposed formulation can reproduce the rate-dependent behaviour of moving contact line, accuracy of the simulation results remains to be investigated. In the following, two forms of empirical power law correlations are used to examine the results. Firstly, the above simulation results with the presence of F_i^{vis} is replotted in Fig. 5.4. Instead of the scattered plot, smoothed density histogram plot is applied to have a clear view of data density distribution. Note that the legend bars represent the relative value of data density, e.g., ‘1.0’ refers to the highest density of data and ‘0.0’ refers to the lowest data density. Then, the power law correlation of Eq. (2.9) in Chapter 2 is used to fit the results and the constants are derived. From literature review we know that the constant B ranges from 0.2 to 1.0 based on experimental findings and theoretical prediction. In our simulation results, B value of 0.531 and 0.406 is derived for advancing and receding cases, respectively, which suggests that our results consist with the above range for B . Here, the quasi-static advancing and receding contact angle (θ_s^a and θ_s^r) are obtained by raising or lowering the bottom substrate with extremely slow velocity of 2×10^{-5} mm/s.

Furthermore, the simulation results can also be compared with the power law correlation proposed by Seebergh and Berg in [44], where the dynamic contact angle and Ca is described as $\frac{|\cos\theta_d^{a/r} - \cos\theta_s^{a/r}|}{(1 + \cos\theta_s^{a/r})} = ACa^B$ and B equals 0.42. An additional term $(1 + \cos\theta_s^{a/r})$ is added to minimize the deviations induced by fluid properties when comparing results of different fluids. Our model also produces a similar range of B agreeing well with the experimental results in [44].

The above verification on our simulation results demonstrated that the model can not only reproduce the rate-dependent behaviours of moving contact line, but also shows good agreement with existing studies in terms of power law correlation fitting constants.

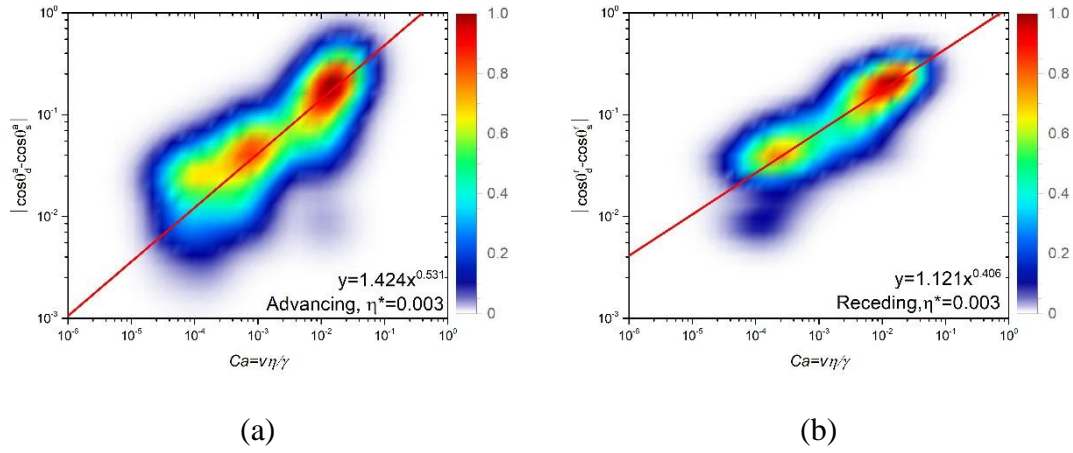


Fig. 5.4 Smooth density histogram plot and power law fitting for dynamic (a) advancing, and (b) receding contact angle results, x and y stands for Ca and $|\cos\theta_d^{a/r} - \cos\theta_s^{a/r}|$ respectively.

5.3 Parametric study of η^*

In this section, we will present the parametric study of the SPH model with respect to the interfacial viscous force \mathbf{F}_i^{vis} . The magnitude of interfacial viscous force \mathbf{F}_i^{vis} can be altered by different value of η^* , which will influence the triple-line region behaviour and dynamic contact angle. In order to study the correlation between interfacial viscous force parameter η^* and resulting dynamic contact angle, five sets of simulations with η^* ranging from 0.006, 0.003, 0.0015, 0.0006 and 0 Pa·s are presented. Each set of simulations are conducted with different substrate speeds, resulting Ca covering from 10^{-6} to 10^{-2} .

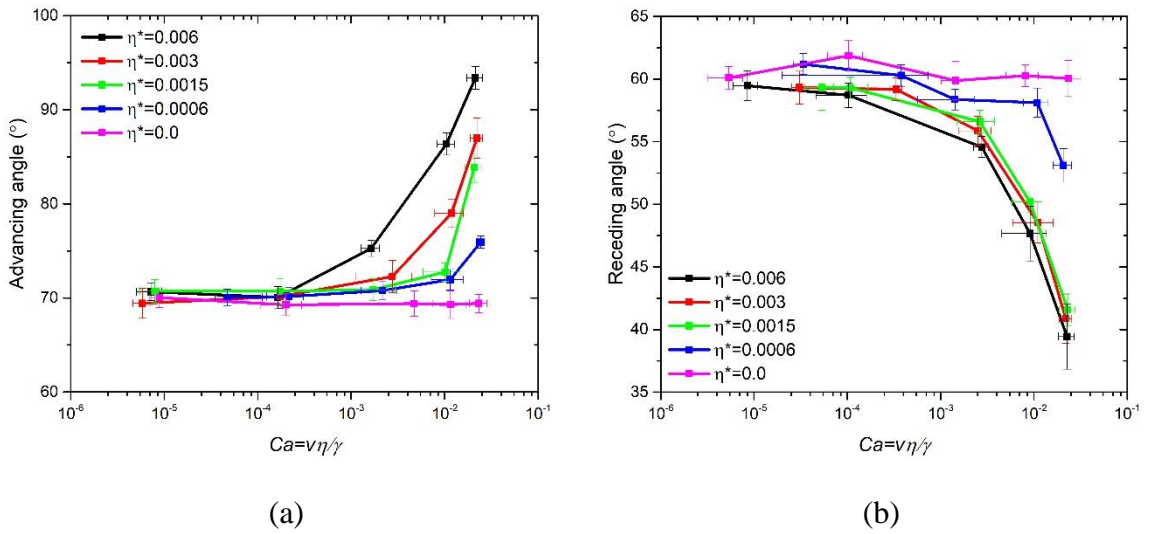


Fig. 5.5 Dynamic contact angle with different magnitude of interfacial viscous force for (a) advancing cases; (b) receding cases.

We selected the simulations with bottom substrate speeds of 20 mm/s, 10 mm/s, 2 mm/s, 0.2 mm/s, 0.02 mm/s and 0.002 mm/s to study the correlation between dynamic contact angle and Ca with different value of η^* . In Fig. 5.5, it can be observed that larger η^* would result a larger advancing angle and smaller receding angle especially in higher Ca regime, which means the contact angle hysteresis is enhanced by the increase of η^* . The largest dynamic advancing angle for five cases are 93.38° , 86.98° , 83.86° , 75.93° , 69.43° respectively, and 39.43° , 40.85° , 41.59° , 53.10° , 61.04° for dynamic receding cases. As Ca is getting smaller, the dynamic advancing and receding angle converge to around 70° and 60° , respectively.

The enhancement of dynamic contact angle on larger value of η^* can be interpreted from the perspective of slip length and surface roughness, and this phenomenon is in good agreement with experiment results. Studies have suggested that the degree of slip is reduced by surface roughness, and the contact angle hysteresis is further enhanced by rough surface [45, 96]. According to Eq. (3.29), the value of η^* is inversely proportional to the slip length L_s in the model. Therefore, the selection of large value η^* refers to a small L_s , which simulates a rougher surface leading to larger contact angle hysteresis. Similarly, a small value of η^* will result in a large slip length, so the surface would be less rough and the contact angle hysteresis is less profound.

Nevertheless, when η^* is larger than 0.0015 Pa·s, there is a little difference between the dynamic advancing and receding angle for substrate moving velocity larger than 10 mm/s. It is observed that the dynamic advancing angle varies 5° to 10° with different η^* value, while the variation for dynamic receding angle is only within 2° . We interpret this phenomenon from the perspective of liquid-solid particle interactions with a strong interfacial viscous force. For the dynamic receding angle case, the solid boundary at triple-line region is emerged in the fluid as pre-wetted surface. In scenarios with a relative large interfacial viscous force, a thin water film is formed and attached on the solid surface and gravity force can hardly drive it downwards, see Fig. 5.6 (a). In this circumstance, the dynamic receding angle is perceived as the intersection between the water film and fluid curvature, and the triple-line region is not strongly influenced by F_i^{vis} . Therefore, the dynamic receding angles tend to be very small and the values are very close. When the moving contact line velocity is smaller, or the interfacial viscous force is less significant, there will be no water film formed on the solid surface as shown in Fig. 5.6 (b). In addition, the thin water film will not form even with strong interfacial viscous force in the advancing angle case, because the surface of the capillary tube is not pre-wetted.

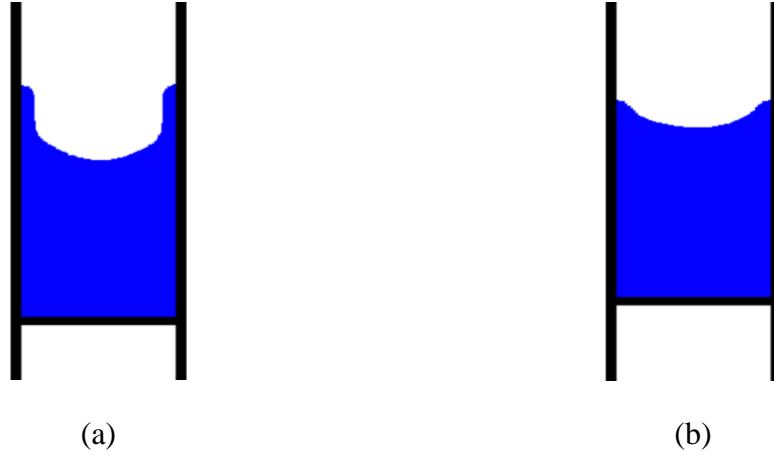


Fig. 5.6 Dynamic receding angle simulation, (a) presence of thin water film with the substrate moving at 20 mm/s; (b) without thin water film with the substrate moving at 2 mm/s.

To obtain a further understanding of how the parameter η^* influences the dynamic contact angle, the simulation results with 5 different η^* values are fitted with Eq. (2.9) and constants A and B are derived correspondingly. Similarly, all scattered data are represented with smooth density histogram. In Fig. 5.7, it is observed that A and B in the power law fitting, which represents amplitude and exponent of the curve, respectively, changes with the value of η^* . For $\eta^* > 0.001$ Pa·s, the slope is quite obvious, the value of $|\cos\theta_d^{a/r} - \cos\theta_s^{a/r}|$ decreases as the decrease of Ca . For $\eta^* = 0.0006$ Pa·s, the slope is not very evident with fitting results giving a small value of B . For the case $\eta^* = 0$ Pa·s, the slope will be 0 as expected since there is no rate-dependent behaviour of contact angle.

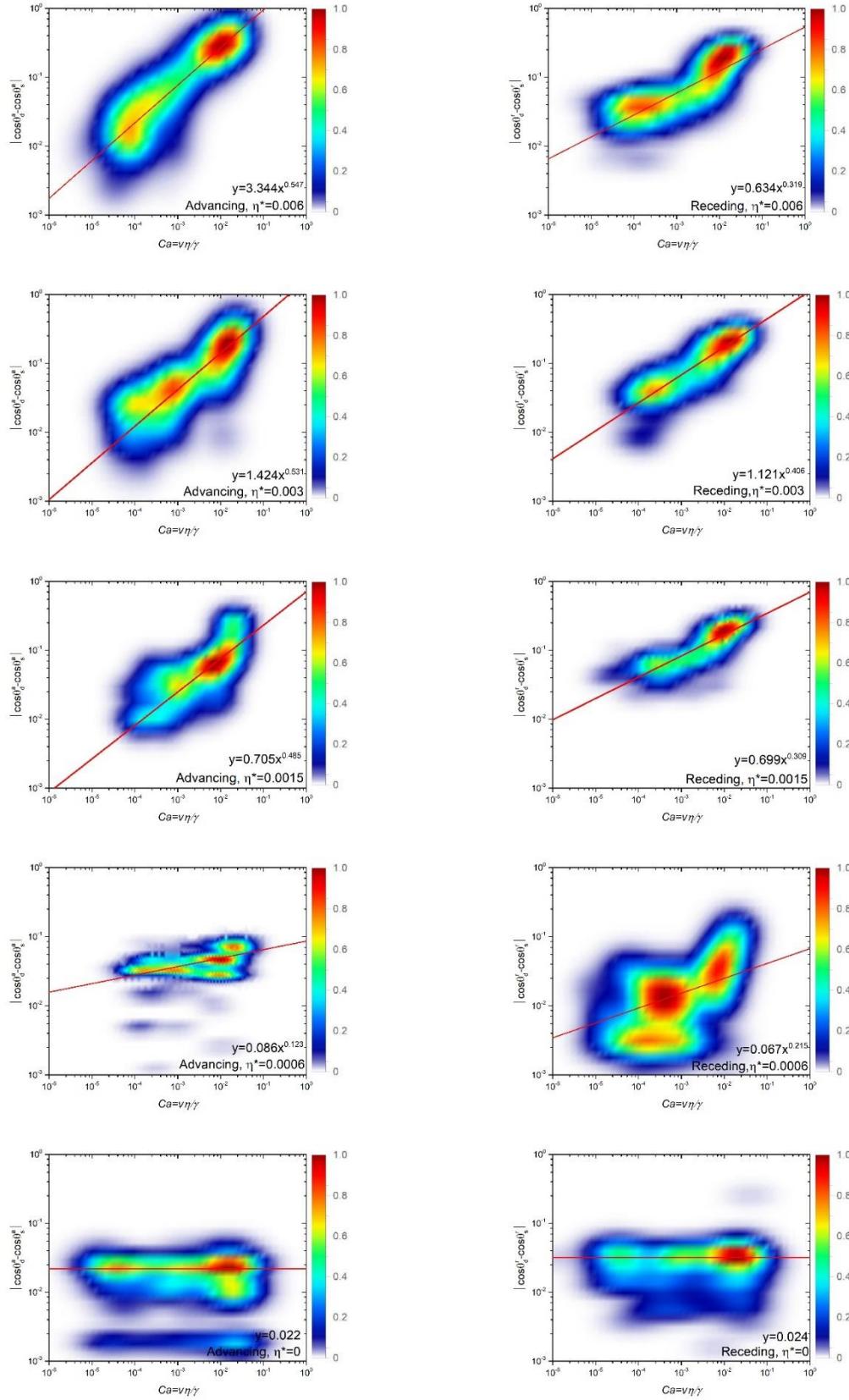


Fig. 5.7 Density histogram plots and power law fitting for dynamic contact angle results with different η^* value, and x and y stands for $|\cos\theta_s^{a/r} - \cos\theta_d^{a/r}|$ and Ca , respectively.

Furthermore, we compared our numerical predictions using $\eta^* = 0.009, 0.006$ and $0.003 \text{ Pa}\cdot\text{s}$ with the empirical power law correlations proposed in [6, 7] and experimental data extracted from [97] that including various combination of liquid and solid materials. Since all these previous studies focused on the dynamic advancing cases for various types of liquid, we used here the additional term $(1 + \cos\theta_s^a)$ to unify the numerical and experimental data, as shown in Fig. 5.8. Excellent agreement is observed between simulation results with $\eta^* = 0.009 \text{ Pa}\cdot\text{s}$ and the experimental data from [97]. In addition, the simulation results using $\eta^* = 0.006 \text{ Pa}\cdot\text{s}$ and $\eta^* = 0.003 \text{ Pa}\cdot\text{s}$ are consistent with the empirical correlations derived by Bracke et al. [7] and Jiang et al [6], respectively. Note that instead of fitting the experimental data using two-parameter power law correlations, our prediction only depends on the value of interfacial viscosity η^* , which has a physical meaning as shown in Eq. (3.29) and can be identified independently from measurements of the apparent slip length. This verification on our simulation results demonstrate that not only the model can reproduce the rate-dependent behaviour of moving contact line, but also a good agreement with existing experimental studies can be achieved.

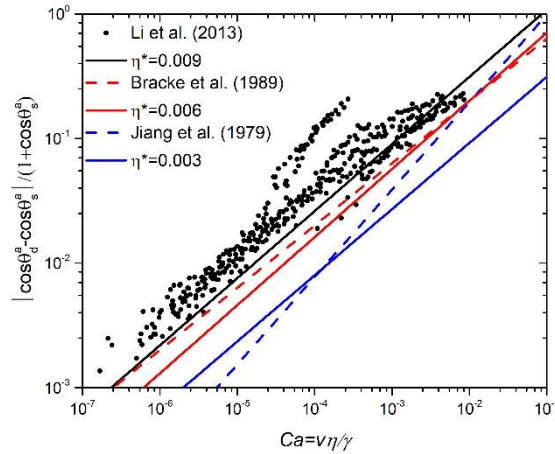


Fig. 5.8 Comparison of power law correlations obtained from simulations with experimental data and empirical power law correlations.

All the fitting results for A and B , amplitude and exponent, respectively, under different magnitude of \mathbf{F}_i^{vis} are plotted in Fig. 5.9. In general, the value of A and B increases with η^* . The only exception is the dynamic receding angle with $\eta^* = 0.006 \text{ Pa}\cdot\text{s}$. The reason is also due to water film caused by the strong adhesion between liquid and solid particles. It can be concluded from our simulation that the value of power law fitting constant B shares a positive correlation with η^* . To further validate the dynamic contact angle simulation results derived from this model, the values of B given by η^* in both advancing and receding cases are

compared with experimental results. In the work of Shi et al. [98], constant B equals 0.17 and 0.16 for advancing and receding scenarios, respectively, based on similar power law function. These two values can be achieved within a narrow range of η^* (around 0.0005 Pa·s) in our model as shown in Fig. 5.9, which suggests the simulation results share good agreement with experimental outcomes within this η^* region.

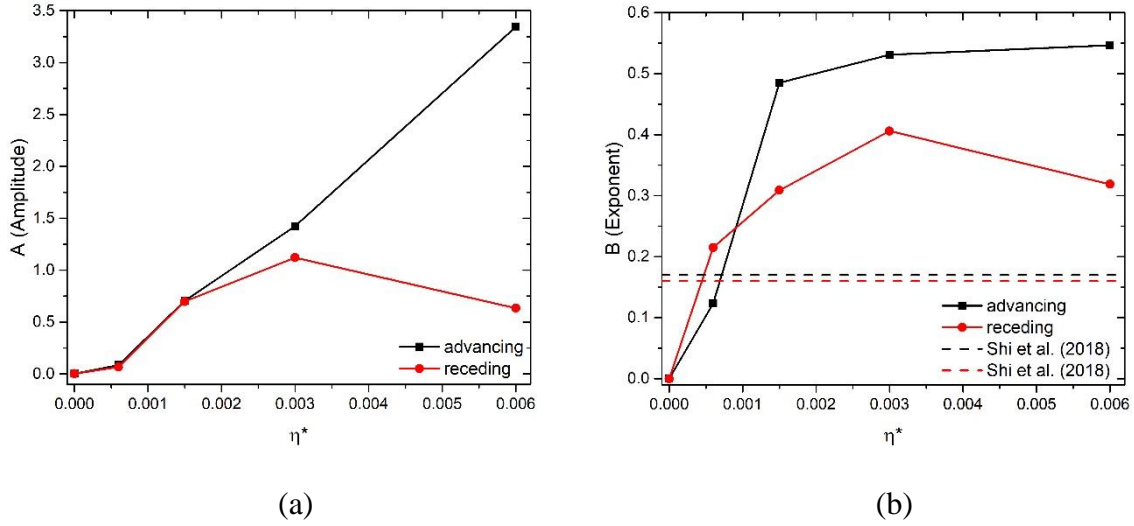


Fig. 5.9 Relationship between power law fitting constants, (a) amplitude and (b) exponent, and η^* .

5.4 Scaling of η^*

As stated in the Chapter 3, to reproduce the dynamic contact angle, the viscosity η at the liquid-solid interface is replaced by the interfacial viscous force parameter η^* , which is related to the slip length and surface roughness at the microscopic scale. In Section 5.3, simulations are conducted with same fluid viscosity and different power law fitting parameters are derived depending on the values of η^* . However, for fluids with different viscosity, the prediction and dependence of dynamic contact angle results on different value of η^* is unknown. We suppose that the ratio of interfacial viscous force parameter η^* and bulk viscosity η , i.e., $\frac{\eta^*}{\eta}$, dominates the power law correlation between dynamic contact angle and Ca , and same value of $\frac{\eta^*}{\eta}$ will reproduce similar simulation results for fluids with different viscosity. To examine the influence of $\frac{\eta^*}{\eta}$ on dynamic contact angle simulation results, two sets of simulations with different bulk viscosity setting (0.013 Pa·s and 0.185 Pa·s) are conducted, and the results are

compared with the $\eta^* = 0.003$ Pa·s case in Section 5.3. All these three cases share same value of $\frac{\eta^*}{\eta} = 0.075$.

The data cover the range of Ca from 10^{-6} to 10^{-1} , and the results are plotted in Fig 5.10. The red line is the fitting function derived from the reference case with $\eta = 0.04$ Pa·s and $\eta^* = 0.003$ Pa·s. The dynamic receding angle case with fluid bulk viscosity 0.185 Pa·s is excluded for discussion, because in this high viscosity setting the interfacial viscous force F_i^{vis} will be quite large with fixed ratio $\frac{\eta^*}{\eta}$, which causes the strong adhesion between liquid and solid particles discussed previously and the accurate contact angle is difficult to determine.

In Fig. 5.10, it is observed that the scattered data of three cases cover different range of Ca as the viscosity is varied. Nonetheless, the data for advancing and receding cases with different bulk viscosity settings can still be described by the reference curve. This result demonstrates that for fluids with different viscosity, the same ratio of $\frac{\eta^*}{\eta}$ will lead to similar dynamic contact angle as well as the corresponding power law fitting results.

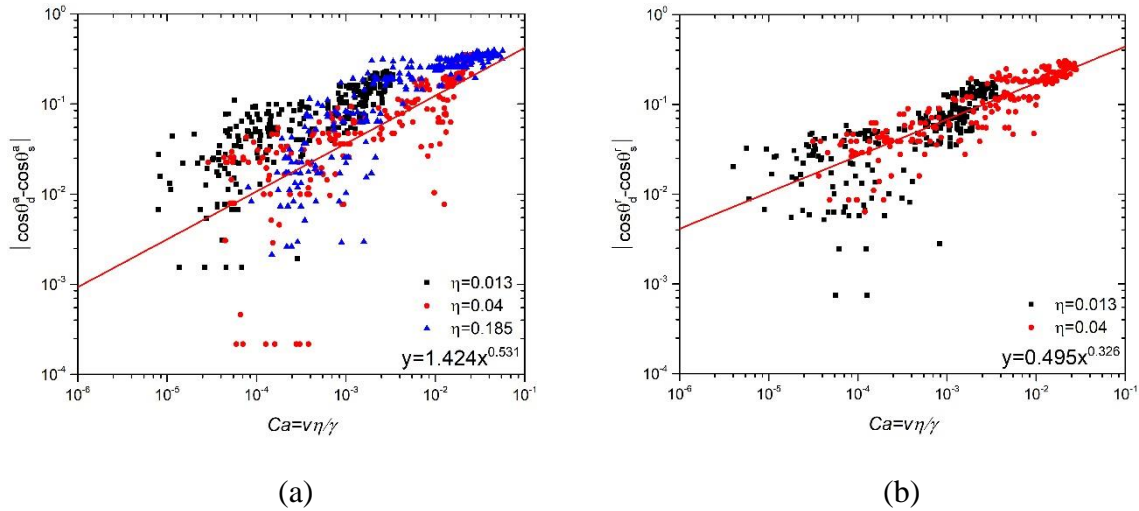


Fig. 5.10 Scattered plot of dynamic contact angles with different viscosity of fluid and

$\frac{\eta^*}{\eta} = 0.075$: (a) advancing angle; (b) receding angle.

5.5 Mesh sensitivity test for F_i^{vis}

Since the interfacial viscous force formulation Eq. (3.30) includes the mesh size L_0 , the mesh sensitivity studies should be conducted. The particle spacing used for the above simulations is $L_0 = 2.5 \times 10^{-5}$ m, and in this sensitivity study, the particle spacing is doubled to $L_0' = 5.0 \times 10^{-5}$ m. The mesh testing case is simulated with the same parameters as the original

mesh case in which the interfacial viscous force parameter η^* equals 0.003 Pa·s, and the results are plotted in Fig. 5.11. To verify the simulation results with doubled particle spacing L_0' , the power law fitting curve derived from original particle spacing L_0 is also plotted as the red reference line in Fig. 5.11 for comparison. It can be observed that for the advancing case, the mesh testing results can be well described by the red line. For the receding case, there are some deviations between the simulation data and reference curve. However, the slope of data is still quite close to the red line. In summary, the mesh scaling in the interfacial viscous force formulation Eq. (3.30) is validated and the dynamic contact angle simulation results are hardly affected by the different choice of particle spacing.

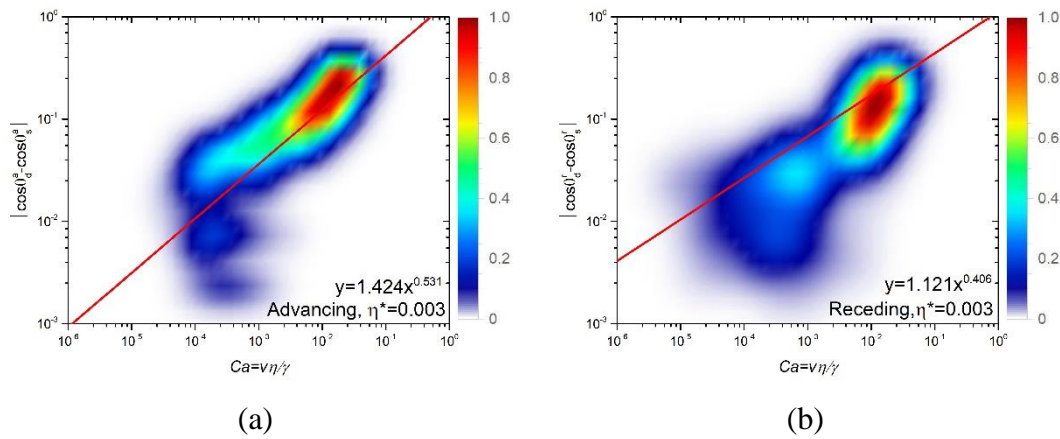


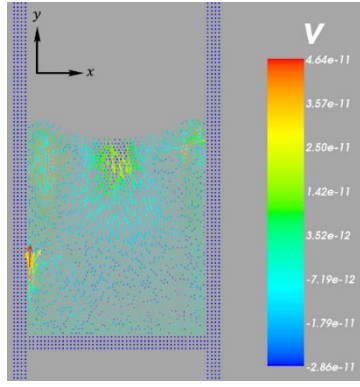
Fig. 5.11 Smooth density histogram plot for dynamic contact angle simulation results with doubled particle spacing L_0' : (a) advancing case; (b) receding case. The red line refers to power law fitting curve with original particle spacing L_0 .

5.6 Velocity field in capillary tubes

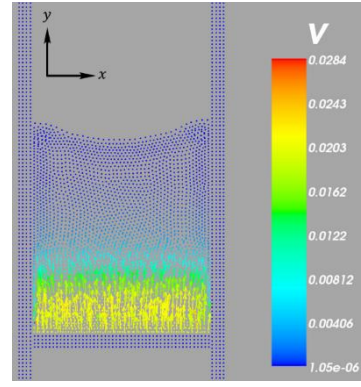
The velocity field plays an important role in understanding the flow motion under dynamic conditions. In experiment, it is very difficult to observe the velocity field of fluid involved in capillary interactions. However, in this numerical model, the velocity field can be visualised by plotting the velocity vector of each liquid particle. The flow condition at the triple-line region can be examined, and the velocity difference between the bulk and interface particles are compared. In this section, the velocity field of dynamic advancing angle simulation with substrate speed of 0.02 m/s is analysed. The snapshots of fluid motion at various simulation time steps are reported in Fig. 5.12.

At $t = 0$ ms, the fluid in the capillary tube is under a quasi-static configuration and the velocity of all liquid particles are smaller than 5×10^{-11} m/s, see Fig. 5.12 (a). The liquid-solid

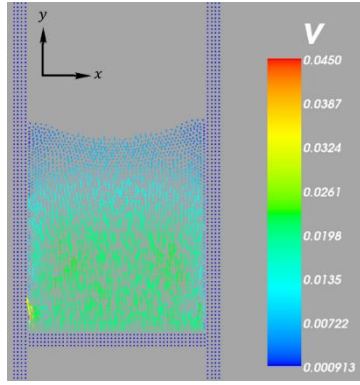
interaction force is set larger than the liquid-liquid interaction force to simulate a hydrophilic surface, so liquid particles at triple-line region will tend to move up slightly while particles in the bulk middle region will tend to move towards the sides. At $t = 0.37$ ms and $t = 0.87$ ms, the bottom substrate starts to move up as shown in Figs. 5.12 (b) and (c), respectively. The velocity is transferred from the substrate to the liquid particles, and this process will take several time steps because the sound speed of the fluid is set to be relative low ($c = 3$ m/s). In addition, we can see that the velocity of liquid particles adjacent to substrate is very close to 0.02 m/s. In Figs. 5.12 (d) and (e), the velocity of substrate has been fully transferred to all liquid particles. These two snapshots suggest that liquid particles in bulk region move faster than the particles near the solid boundary, because the interfacial viscous force \mathbf{F}_i^{vis} constrains the motion of liquid particles at interface. Due to the velocity difference of liquid particles at liquid front, the fluid curvature starts to evolve which results the change of contact angle. When the curvature becomes stable under this dynamic condition, the velocity of middle region particles is still larger than the particles near the boundary, but the difference is relatively small compared to previous two snapshots, see Fig. 5.12 (f). There are also some exceptions when the liquid particles are striding over solid particles at the boundary, as shown in Fig. 5.12 (g). Mostly a liquid particle next to the solid boundary tends to stay between two solid particles because the total system energy is comparably small and the force is balanced. However, since the substrate is pushing the fluid upward, the liquid particle need to accumulate enough energy to overcome the boundary repulsive force then move up. In this circumstance, the velocity of these liquid particles could be larger than other liquid particles.



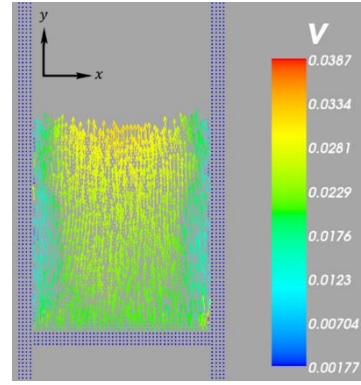
(a) $t = 0$ ms



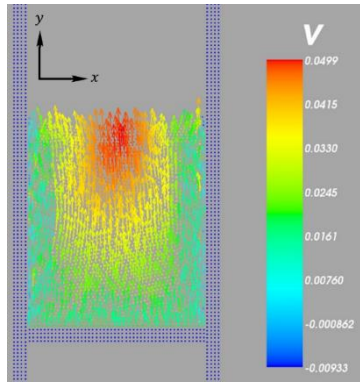
(b) $t = 0.37$ ms



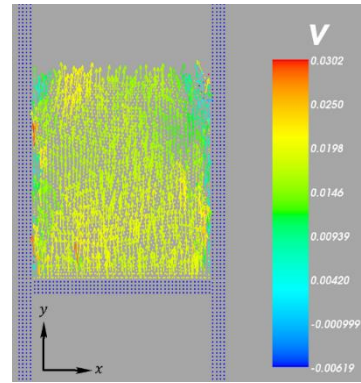
(c) $t = 0.87$ ms



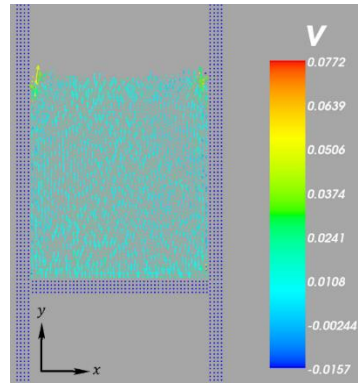
(d) $t = 1.33$ ms



(e) $t = 2.78$ ms



(f) $t = 19.0$ ms



(g) $t = 19.48$ ms

Fig. 5.12 Snapshots of velocity field in a dynamic advancing angle simulation process.

5.7 Summary

In this chapter, we first test the influence of the newly-introduced interfacial viscous force \mathbf{F}_i^{vis} on dynamic contact angle simulations. It is found that the rate-dependent behaviour of moving contact line can be reproduced by including \mathbf{F}_i^{vis} in the momentum equation. Subsequently, different magnitude of \mathbf{F}_i^{vis} is implemented in the model, and power law correlations are derived for each case. The results suggest that the dynamic contact angle and the corresponding power law fitting results are dependent on the introduced interfacial viscous force parameter η^* , where the larger η^* will lead larger constants (amplitude and exponent) in power law fitting. Fluids with different bulk viscosity are also included in the dynamic contact angle simulation, and it turns out that same value of $\frac{\eta^*}{\eta}$ will results similar rate-dependent behaviour of contact angle. Moreover, the mesh sensitivity tests are conducted, and the flow velocity field of dynamic advancing angle simulation is also discussed to characterise the curvature shape evolution process.

Chapter 6

Dynamic Behaviour of Stretching Liquid Bridges

In this chapter, the SPH model with modified Equation of State (EOS) is applied to simulate the stretch and rupture of a liquid bridge under dynamic loading. The shapes and rupture modes of the stretched liquid bridge are presented under different stretching speeds and wettability of the substrates. By differentiating the wettability of substrates, the liquid transfer ratio is studied with respect to the stretching speed and compared with available experimental observations and theoretical predictions. Furthermore, the flow structure of a liquid bridge during the stretching process is presented and discussed.

6.1 A modified EOS for liquid rupture

First, we test the original EOS for simulating liquid rupture phenomena using a simple liquid bridge example. Two parallel substrates with fluid in between are modelled in vacuum to study the stretching and rupture of the liquid bridge. The size of the substrate is $2.6 \text{ mm} \times 0.1 \text{ mm}$, and liquid particles are placed between two substrates occupying the domain of $1.6 \text{ mm} \times 1.0 \text{ mm}$. At simulation time zero ($t = 0 \text{ ms}$), the contact angles that fluid contacting with both top and bottom substrates are 90° , which makes the liquid bridge a rectangular shape, see Fig. 6.1 (a). With the liquid-liquid and liquid-solid interaction forces, the curvature of the liquid bridge evolves to either concave or convex depending on the static contact angle prescribed by the liquid-solid interaction force parameter, as shown in Fig. 6.1 (b). By observing the potential energy fluctuation of the system, it is considered the system is in stable configuration after simulation time 0.2 s and the substrates can only move after this stable condition is achieved. In the following sections, simulation time zero ($t = 0 \text{ ms}$) refers to the time when the stable configuration of the liquid bridge system is achieved.

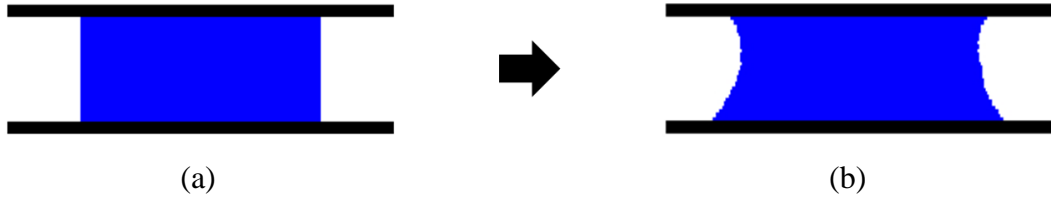


Fig. 6.1 Curvature of liquid bridge at (a) initial configuration; (b) stable configuration.

The SPH equations and parameters in Chapter 3 are used to simulate the rupture of liquid bridge. The upper substrate moves up with constant velocity of 15 cm/s and the position of bottom one is fixed. However, with the stretch of the liquid bridge, it is observed that the curvature became a straight line, and the liquid bridge is not ruptured till the end of simulation, see Fig. 6.2. Subsequently, different stretching speed and wettability of substrate are tested, and the surface tension of simulated fluid is altered, however, the liquid bridge still cannot break.

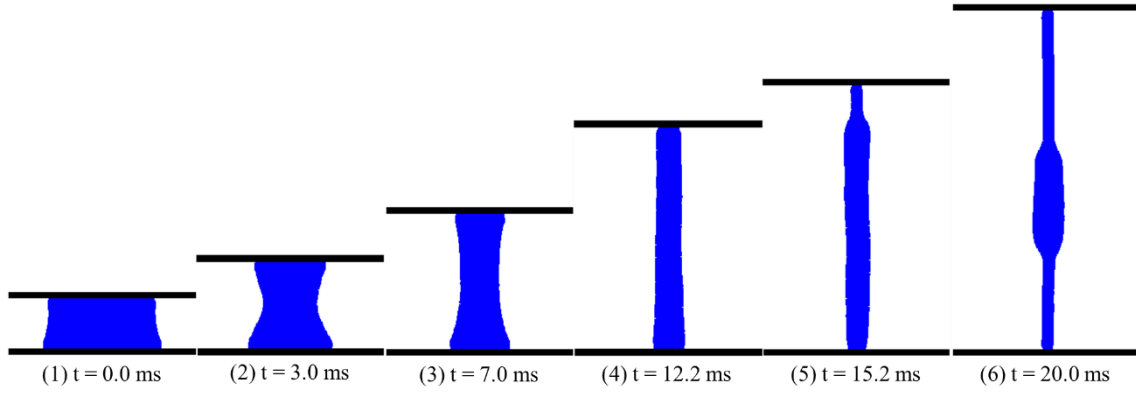


Fig 6.2 Shapes of a liquid bridge at various simulation time with Tait EOS.

To figure out this problem, the density and pressure profile of the stretched liquid bridge are given in Fig. 6.3, and the force balance of liquid bridge is analysed. In this system, there are three forces contributing to the liquid bridge: (1) liquid-solid particle interaction force that resulting the adhesion force between substrates and fluid, (2) liquid-liquid particle interaction force, and (3) pressure-gradient force. The adhesion force is dominating the stretching process so the liquid bridge is stretched. However, due to the boundary deficiency, the pressure of liquid particles at the surface of liquid bridge is negative and the pressure inside the liquid bridge is positive. This provides a strong horizontal pressure-gradient force that resists the deformation of fluid on the horizontal direction, so the liquid bridge can only be extended vertically and hardly get ruptured.

According to the EOS in Chapter 3, Eq. (3.16), the pressure is calculated based on the density of liquid particle ρ_i . When ρ_i is larger than the reference density of fluid ρ_0 , the calculated pressure is positive, and the pressure is negative if ρ_i is smaller than ρ_0 . The reference density

ρ_0 is set as 1000 kg/m^3 for above simulation, while because of the boundary deficiency, the density of some particles drops below 1000 kg/m^3 thus resulting an unphysical negative pressure. As a result, the EOS should be modified to avoid negative pressure, so the adhesion force can break the liquid bridge.

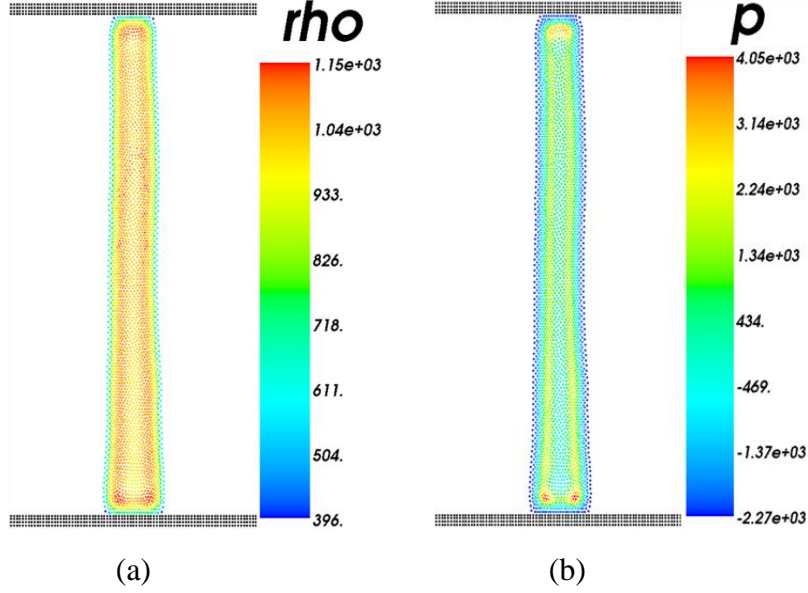


Fig. 6.3 (a) Density and (b) pressure distribution of a stretched liquid bridge with Tait EOS.

Followed by the work of Hughes and Graham [99], an additional criterion is applied on current EOS:

$$\rho_i = \begin{cases} \rho_i, & \rho_i \geq \rho_0 \\ \rho_0, & \rho_i < \rho_0 \end{cases} \quad (6.1)$$

In the original work in [99], this condition is initially applied on boundary particles to prevent sticking behaviour. In our work, adding this criterion can guarantee the minimum pressure of liquid particle non-negative by imposing a minimum value of the density ρ_0 on all liquid particles. This additional constrain does not alter the conclusions from the numerical simulations carried out in Chapter 5, due to the dominance of compressive states in capillary tubes. With this modified EOS, the liquid bridge rupture simulation is conducted under same configuration as previous one, and the stretching process is described in Fig. 6.4.

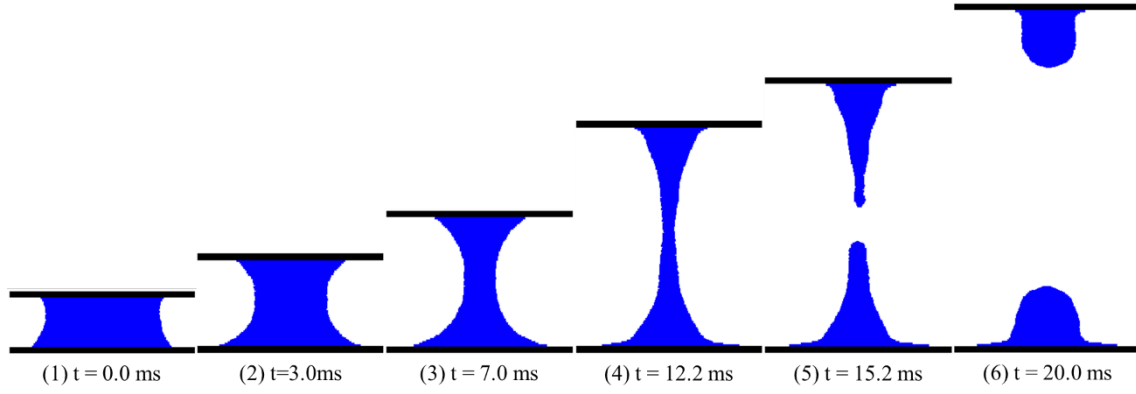


Fig. 6.4 Shapes of a liquid bridge at various simulation time with modified Tait EOS.

Firstly, the curvature of liquid bridge at stable configuration is slightly different from the previous simulation because of the additional condition on pressure prescription. With the stretch of the substrates, the curvature is more like an arc shape and the neck radius is decreasing from $t = 0$ ms to $t = 12.2$ ms. At simulation time $t = 15.2$ ms, the liquid bridge is finally broken into two parts. Afterwards, the liquid particles draw together due to the surface tension effects and inertia effects.

To understand the mechanism of liquid bridge rupture with this modified EOS, the density and pressure profile is shown in Fig. 6.5. The density profile is quite similar with Fig. 6.3 where the fluid density in the bulk region is close to ρ_0 , and the density of liquid particles without sufficient supporting domain is far below 1000 kg/m^3 . Nevertheless, compared with Fig. 6.3, some major differences can be found in pressure profile. The pressure of all liquid particles is non-negative because of the additional criterion of EOS. In addition, the overall pressure is much lower than the previous case, and the pressure of out layer liquid particles is zero. Since the pressure in the liquid bridge neck region is zero, the pressure gradient term in the governing equation is also zero. Therefore, there is no pressure-gradient force to counterbalance the adhesion force from the substrates, so the liquid bridge ruptures as the liquid bridge is stretched upon certain height.

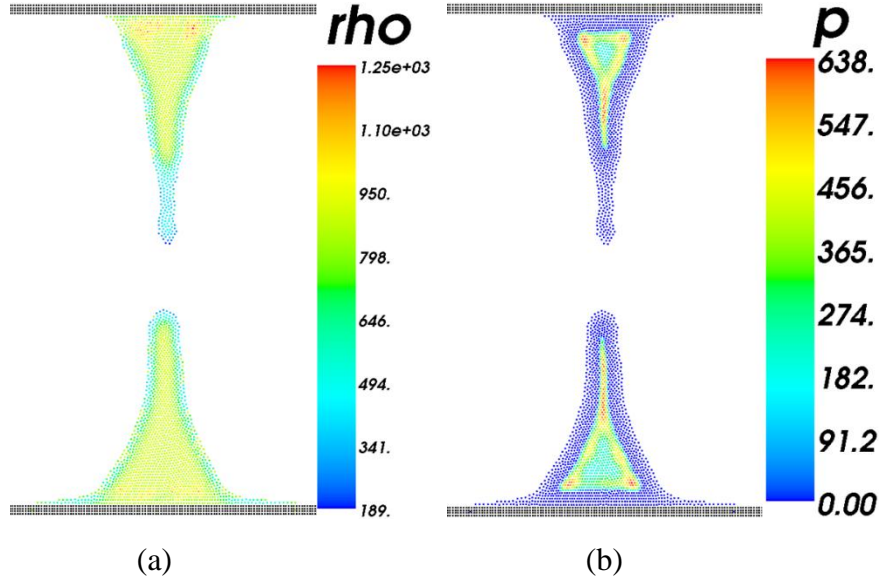


Fig. 6.5 (a) Density, and (b) pressure distribution of a stretched liquid bridge with corrected EOS.

6.2 Rate-dependent behaviour of a stretching liquid bridge

As stated in Chapter 2, the shape and transfer ratio of a liquid bridge depends on both stretching speed and wettability of substrates. In this section, we will firstly examine the shape evolution and rupture modes by simulating three sets of liquid bridge with different wettability under various stretching speeds.

The geometry and parameters are same as those used in Section 6.1, and the static contact angle θ_s of both top and bottom substrates are set to 40° , 60° and 80° . The liquid bridge is stretched at various velocities from 5 cm/s to 20 cm/s with only moving the top substrate, and all results are compared when the distance between two substrates reaches 0.3 cm, in Fig. 6.6.

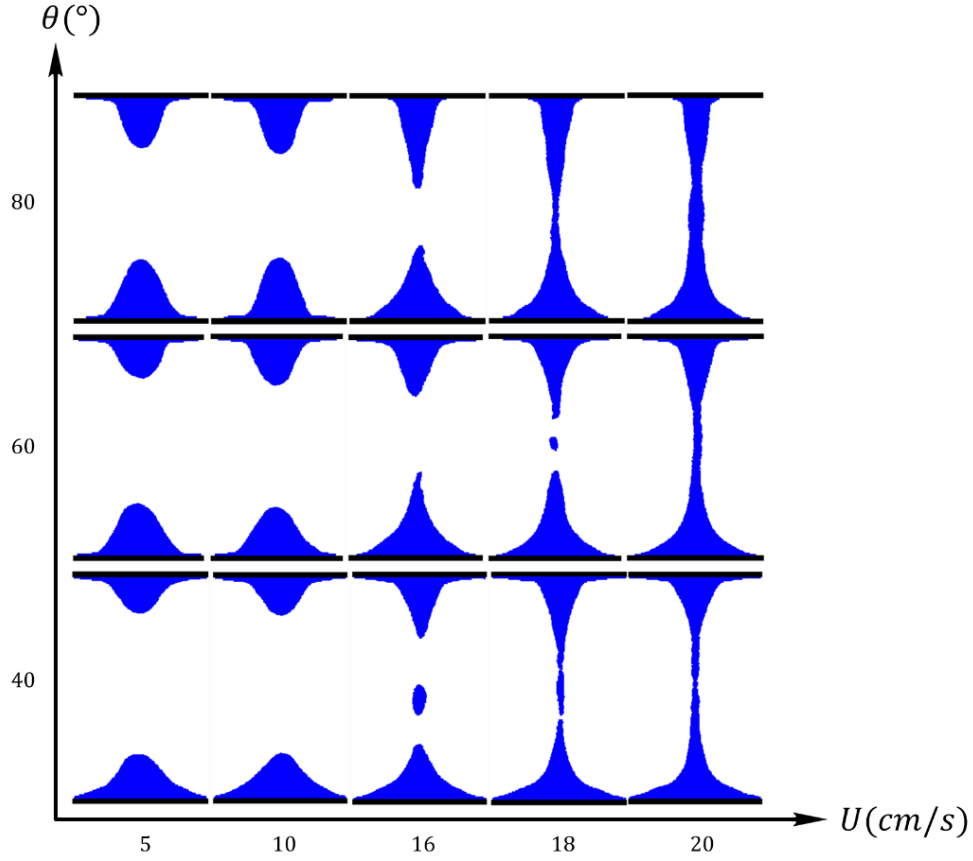
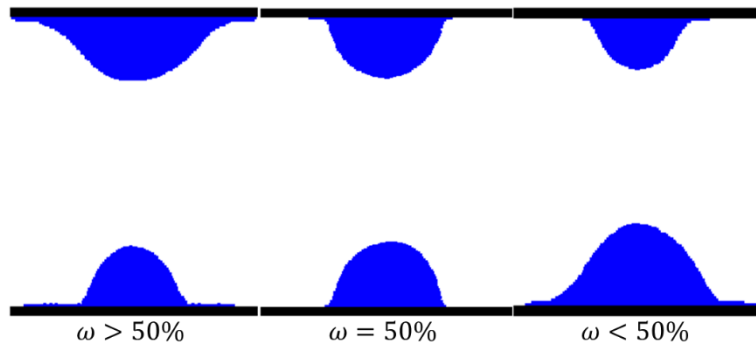


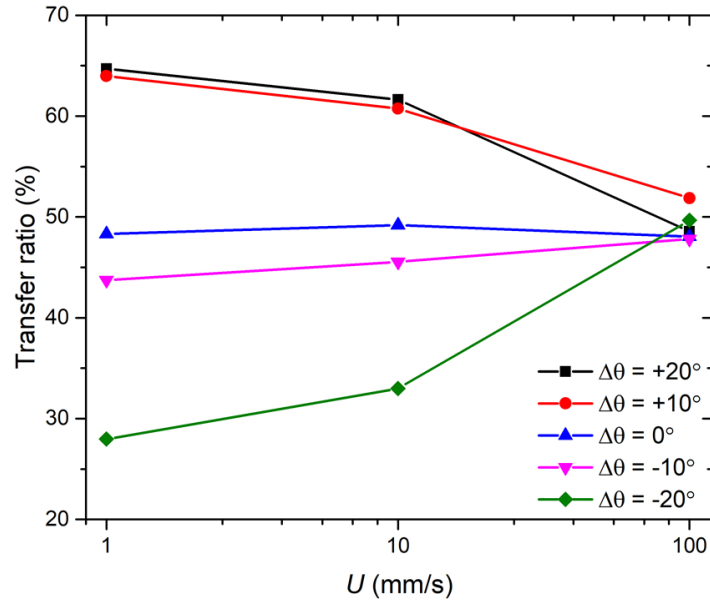
Fig. 6.6 Liquid bridge stretch simulations snapshots for various substrate wettability and moving speeds.

Firstly, the influence of substrate wettability and stretching speeds on the liquid bridge shape is analysed. According to the simulation results at the same final height, three different types of liquid bridge shape are identified with the increase of substrate moving speed: ruptured, droplet in the middle, and not ruptured. Take the $\theta_s = 60^\circ$ for example, the liquid bridge is ruptured for $U \leq 18$ cm/s and not ruptured for $U = 20$ cm/s, and a droplet is formed in the middle when $U = 18$ cm/s. However, this diagram might be different if the wettability of substrates is altered. In the case where θ_s is decreased to 40° , the droplet appears for $U = 16$ cm/s instead of 18 cm/s, and the liquid bridge just ruptured at $U = 20$ cm/s. For the simulation with $\theta_s = 80^\circ$, no droplet formed during stretching process, and the liquid bridge is not ruptured at $U = 18$ cm/s. This diagram suggests that the liquid bridge is ruptured at lower stretching speeds, and not ruptured at higher stretching speed, at the same final height. In addition, if the liquid bridge is ruptured at a relative high stretching speed, a droplet may form in the middle of the liquid bridge. In conclusion, the results indicate that the shape of liquid bridge depends on both the stretching speed and the wettability of substrate. This results qualitatively consist with experimental observations from [54, 55, 100].

In the following, five sets of liquid bridge transfer ratio simulations are conducted. The liquid bridge geometry and parameters in Section 6.1 is used for this simulation. The static contact angle of top substrate θ_t is fixed to 40° , and the wettability of bottom substrate θ_b is varied from 20° to 60° . Three different stretching speeds, $U = 1$ mm/s, 10 mm/s and 100 mm/s are applied on both substrates, with the top substrate moving upwards and bottom substrate moving downwards. When the liquid bridge is ruptured, the transfer ratio ω is calculated as the ratio between the number of liquid particles attached on the top substrate and number of total liquid particles. The image processing for liquid particles counting is detailed in Appendix B. The results for the transfer ratio simulation are plotted in Fig. 6.7.



(a)



(b)

Fig. 6.7 (a) Snapshots of liquid bridge with different transfer ratios; (b) Relationship between liquid bridge transfer ratio and U for $\theta_t = 40^\circ$ and θ_b is varied, $\Delta\theta = \theta_b - \theta_t$.

In Fig 6.7 (a), it is observed that the shape and transfer ratio of liquid bridge varies with the wettability of bottom substrate, and more details can be found in Fig 6.7 (b). When U is 1 mm/s which is the smallest substrate moving speed in this simulation, ω increases with the increase of θ_b . As U increases to 10 mm/s, the transfer ratio still changes monotonically with θ_b , but the range of ω is narrowed compared with the $U = 1$ mm/s case. When U reaches 100 mm/s, the transfer ratio ω for all five cases converge to around 50%. In addition, for the case where θ_b is 40° , the transfer ratio is around 50% for all three substrate moving speeds. The simulation results suggest that in the quasi-static and transition regime, the wettability of substrate dominates the liquid transfer ratio. While in dynamic regime, ω is independent of θ_b and converge to 50% for all cases. The simulation results are compared with experimental observations and other simulation results in [54, 101, 102], and it turns out this model can qualitatively capture the liquid bridge rupture and transfer properties.

6.3 Flow condition in liquid bridges

Current studies focusing on the liquid transfer process and mechanism rarely involve the flow condition and velocity field of a stretched liquid bridge due to the difficulty of experimentally observation. Similar to the flow condition examination conducted in Section 5.6, the flow condition and velocity field of a stretched liquid bridge is examined in this section. The liquid bridge rupture simulation case of Fig. 6.3 ($\theta_b = 60^\circ$, $U = 18$ cm/s) is used for flow condition analysis where the liquid bridge is stretched only by top substrate.

At the beginning of the stretching process, the velocity is transferred from top substrate to the liquid particles, see Fig. 6.8 (a). It also takes hundreds of time steps for the velocity fully transferred to all liquid particles. Subsequently in Fig. 6.8 (b) and (c), the curvature of the liquid bridge starts to evolve under the surface tension effects, and the liquid particles at the edge of bridge tend to move to the centre then move upward. As the neck radius getting smaller, the particle velocity at bottom half region becomes negligible compared with the upper half part.

In Fig. 6.8 (d), when the liquid bridge neck is very thin and about to break, there are vortex formed just below the bridge neck region, which indicates the change of flow velocity direction for bottom part particles. In Fig. 6.8 (e), the flow direction for upper and bottom is opposite to each other, and the liquid bridge finally ruptured in Fig. 6.8 (f). A droplet is formed due to the velocity difference between its adjacent liquid particles, and the droplet is slowly moving up because of inertia.

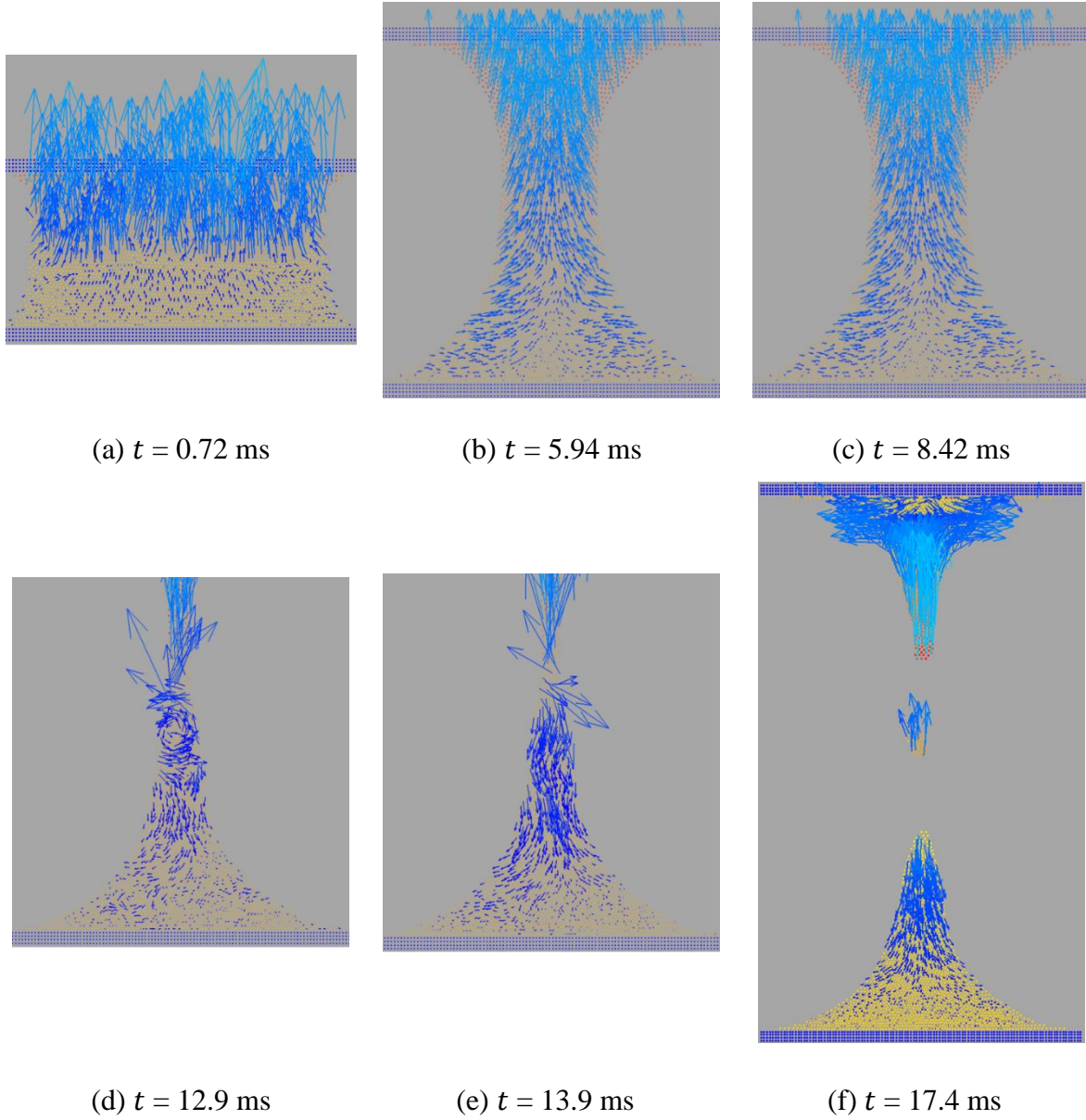


Fig. 6.8 Velocity field of a stretched liquid bridge at various simulation time steps.

6.4 Summary

In this chapter, the rate-dependent behaviour of stretched liquid bridge is simulated and discussed. A modified EOS that avoids negative pressure of liquid particle is applied in the model to properly reproduce the breakage of a stretched liquid bridge. The different rupture modes and transfer ratio of stretched liquid bridges with various substrate wettability and stretching speeds are simulated and analysed, in which the outcomes are agree well with experimental and other simulation results. In addition, the flow condition and velocity field of a stretched liquid bridge is also presented and discussed. These preliminary analyses warrant an improved modelling approach for future studies on dynamic behaviour of liquid bridges.

Chapter 7

Conclusion and Future Work

7.1 Conclusion

This thesis numerically investigated the properties of capillary interactions with emphasis on the contact angle dynamics and stretching process of liquid bridges. A modified SPH model with inter-particle and interfacial viscous force is applied to simulate the rate-dependent contact angle behaviour. A capillary tube with a shifting bottom substrate is simulated and the dynamic contact angle is reproduced by raising or withdrawing liquid particles inside the tube. Various simulations are proceeded to verify the effectiveness of this newly-introduced interfacial viscous force, \mathbf{F}_i^{vis} , and parametric study of the interface viscosity, η^* , is also conducted. In addition, the EOS of the model is modified particularly for reproducing the rupture of a stretching liquid bridge, followed by studies on the shape evolution as well as transfer ratio.

The main conclusions are as follows:

1. The interface of fluids with different surface tension, and surfaces with different wettability can be reproduced by the particle-particle interaction force formulation. Under the current SPH framework, model parameters can be identified from the intrinsic material properties, including the surface tension, static contact angle, and viscosity of the simulated fluid.
2. To study the dynamic capillary interactions, it is demonstrated that the rate-dependent behaviour only occurs with the implementation of the interfacial viscous force, \mathbf{F}_i^{vis} , introduced in the work. The simulation results consist with different forms of power law correlation describing the dynamic contact angle as function of Ca . The influence of different magnitude of \mathbf{F}_i^{vis} on the contact angle dynamics is also studied, in which the power law fitting constants change monotonically with the interfacial viscosity parameter η^* . This finding is interpreted from the perspective of correlations between η^* , slip length and microscopic surface roughness. It is shown that the increase of η^* will lead to larger contact angle hysteresis, and this dependency is further explained from the perspective of correlations between η^* , slip length and surface roughness. The viscosity ratio, $\frac{\eta^*}{\eta}$, is proved to be responsible for achieving similar dynamic contact angle behaviours even with fluids

having different viscosity. In addition, velocity field of the flow inside capillary tube is presented and discussed, in which the velocity of triple-line region and bulk region is compared to account for the formation of dynamic contact angle.

3. Moreover, a modified EOS is implemented in the model to reproduce the rupture of a stretched liquid bridge. Utilising this EOS, the rupture mode of liquid bridge is found to depend on the substrate moving velocity and wettability. Moreover, the transfer ratio of a stretched liquid bridge under various loading rates and wettability is studied and the results are comparable to experimental and theoretical values. The flow condition and velocity field are also provided for further understanding the mechanism of a stretched liquid bridge upon rupture.

This study provides a comprehensive investigation on contact angle dynamics and liquid bridge properties under dynamic loading conditions. Under this modified SPH model, the rate-dependent behaviours of contact angle are successfully reproduced. The interfacial viscous force formulation is further demonstrated to share physical links to slip length and microscopic roughness of surface. The results derived from this modified SPH model can be applied into a variety of industrial and geological applications where dynamic capillary interactions usually occur, including carbon geosequestration, oil recovery, porous catalysis, and groundwater treatment.

7.2 Future work

The findings in hysteretic behaviours of capillary interactions from this thesis stimulate further work in the following aspects:

- (1) The simulation results in this work suggest that the parameter η^* , which can be related to the slip length and surface roughness, shares monotonic relationship with power law exponent, B . However, experimental observations regarding this correlation are scarcely found. Therefore, further experimental identification of the correlation between surface roughness and power law exponent B is required to verify the findings derived from this work.
- (2) The numerical model in this work can only qualitatively capture the transfer ratio of a stretching liquid bridge. At quasi-static regime, deviations are observed when comparing the transfer ratio results with experimental values. As a result, the model for liquid transfer ratio simulation should be improved to quantitatively reproduce the liquid motion at quasi-

static regime. In addition, the effect of surface roughness on liquid bridge transfer ratio is of great interest to be investigated.

References

- [1] K. Pruess and J. Garcia, "Multiphase flow dynamics during CO₂ disposal into saline aquifers," *Environmental Geology*, vol. 42, pp. 282-295, 2002.
- [2] L. M. Abriola and G. F. Pinder, "A multiphase approach to the modeling of porous media contamination by organic compounds: 1. Equation development," *Water resources research*, vol. 21, pp. 11-18, 1985.
- [3] F. Orr and J. Taber, "Use of carbon dioxide in enhanced oil recovery," *Science*, vol. 224, pp. 563-570, 1984.
- [4] L. Kiwi-Minsker and A. Renken, "Microstructured reactors for catalytic reactions," *Catalysis today*, vol. 110, pp. 2-14, 2005.
- [5] A. M. Schwartz and S. B. Tejada, "Studies of dynamic contact angles on solids," *Journal of Colloid and Interface Science*, vol. 38, pp. 359-375, 1972.
- [6] T.-S. Jiang, O. Soo-Gun, and J. C. Slattery, "Correlation for dynamic contact angle," *Journal of Colloid and Interface Science*, vol. 69, pp. 74-77, 1979.
- [7] M. Bracke, F. De Voeght, and P. Joos, "The kinetics of wetting: the dynamic contact angle," *Trends in Colloid and Interface Science III*, pp. 142-149, 1989.
- [8] R. Cox, "The dynamics of the spreading of liquids on a solid surface. Part 1. Viscous flow," *Journal of Fluid Mechanics*, vol. 168, pp. 169-194, 1986.
- [9] R. L. Hoffman, "A study of the advancing interface: II. Theoretical prediction of the dynamic contact angle in liquid-gas systems," *Journal of Colloid and Interface Science*, vol. 94, pp. 470-486, 1983.
- [10] P. Raiskinmäki, A. Shakib-Manesh, A. Jäsberg, A. Koponen, J. Merikoski, and J. Timonen, "Lattice-Boltzmann simulation of capillary rise dynamics," *Journal of statistical physics*, vol. 107, pp. 143-158, 2002.
- [11] J. Koplik, J. R. Banavar, and J. F. Willemsen, "Molecular dynamics of Poiseuille flow and moving contact lines," *Physical review letters*, vol. 60, p. 1282, 1988.
- [12] M. Huber, F. Keller, W. Säckel, M. Hirschler, P. Kunz, S. M. Hassanizadeh, *et al.*, "On the physically based modeling of surface tension and moving contact lines with dynamic contact angles on the continuum scale," *Journal of Computational Physics*, vol. 310, pp. 459-477, 2016.
- [13] E. Schäffer and P.-z. Wong, "Contact line dynamics near the pinning threshold: A capillary rise and fall experiment," *Physical Review E*, vol. 61, p. 5257, 2000.
- [14] T. Blake and J. Haynes, "Kinetics of liquid-liquid displacement," *Journal of colloid and interface science*, vol. 30, pp. 421-423, 1969.
- [15] P. Petrov and I. Petrov, "A combined molecular-hydrodynamic approach to wetting kinetics," *Langmuir*, vol. 8, pp. 1762-1767, 1992.
- [16] P. Meakin and A. M. Tartakovsky, "Modeling and simulation of pore - scale multiphase fluid flow and reactive transport in fractured and porous media," *Reviews of Geophysics*, vol. 47, 2009.
- [17] P. A. Thompson and M. O. Robbins, "Simulations of contact-line motion: slip and the dynamic contact angle," *Physical Review Letters*, vol. 63, p. 766, 1989.
- [18] A. V. Lukyanov and A. E. Likhtman, "Dynamic Contact Angle at the Nanoscale: A Unified View," *ACS nano*, vol. 10, pp. 6045-6053, 2016.
- [19] L. O. Dos Santos, F. G. Wolf, and P. C. Philippi, "Dynamics of interface displacement in capillary flow," *Journal of statistical physics*, vol. 121, pp. 197-207, 2005.

- [20] S. Chibbaro, L. Biferale, F. Diotallevi, and S. Succi, "Capillary filling for multicomponent fluid using the pseudo-potential Lattice Boltzmann method," *The European Physical Journal-Special Topics*, vol. 171, pp. 223-228, 2009.
- [21] A. M. Tartakovsky and A. Panchenko, "Pairwise force smoothed particle hydrodynamics model for multiphase flow: surface tension and contact line dynamics," *Journal of Computational Physics*, vol. 305, pp. 1119-1146, 2016.
- [22] A. Caiazzo, "Analysis of lattice Boltzmann nodes initialisation in moving boundary problems," *Progress in Computational Fluid Dynamics, an International Journal*, vol. 8, pp. 3-10, 2008.
- [23] P.-G. De Gennes, F. Brochard-Wyart, and D. Quéré, *Capillarity and wetting phenomena: drops, bubbles, pearls, waves*: Springer Science & Business Media, 2013.
- [24] H. Bruus, *Theoretical microfluidics*: Oxford university press Oxford, 2007.
- [25] Available: <http://www.ramehart.com/contactangle.htm>
- [26] T. Young, "An essay on the cohesion of fluids," *Philosophical Transactions of the Royal Society of London*, vol. 95, pp. 65-87, 1805.
- [27] P. S. Laplace, "Theory of capillary attraction." Supplements to the 10th book of Celestial Mechanics," *Supplements to the 10th book of Celestial Mechanics*, 1807.
- [28] C. Navier, "Mémoire sur les lois du mouvement des fluides," *Mem. Acad. Sci. Inst. Fr*, vol. 6, pp. 389-416, 1823.
- [29] E. Lauga, M. Brenner, and H. Stone, "Microfluidics: the no-slip boundary condition," in *Springer handbook of experimental fluid mechanics*, ed: Springer, 2007, pp. 1219-1240.
- [30] R. Pit, H. Hervet, and L. Leger, "Direct experimental evidence of slip in hexadecane: solid interfaces," *Physical review letters*, vol. 85, p. 980, 2000.
- [31] J. P. Rothstein, "Slip on superhydrophobic surfaces," *Annual Review of Fluid Mechanics*, vol. 42, pp. 89-109, 2010.
- [32] M. Majumder, N. Chopra, R. Andrews, and B. J. Hinds, "Nanoscale hydrodynamics: enhanced flow in carbon nanotubes," *Nature*, vol. 438, pp. 44-44, 2005.
- [33] C. Lee and C.-J. C. Kim, "Maximizing the giant liquid slip on superhydrophobic microstructures by nanostructuring their sidewalls," *Langmuir*, vol. 25, pp. 12812-12818, 2009.
- [34] Y. Yuan and L. T. Randall, "Contact angle and wetting properties," in *Surface science techniques*, ed: Springer Berlin Heidelberg, 2013.
- [35] C. W. Extrand, "Contact angles and hysteresis on surfaces with chemically heterogeneous islands," *Langmuir*, vol. 19, pp. 3793-3796, 2003.
- [36] G. Elliott and A. Riddiford, "Dynamic contact angles: I. The effect of impressed motion," *Journal of colloid and interface science*, vol. 23, pp. 389-398, 1967.
- [37] T. Nattermann, S. Stepanow, L.-H. Tang, and H. Leschhorn, "Dynamics of interface depinning in a disordered medium," *Journal de Physique II*, vol. 2, pp. 1483-1488, 1992.
- [38] T. E. Mumley, C. Radke, and M. C. Williams, "Kinetics of liquid/liquid capillary rise: I. Experimental observations," *Journal of colloid and interface science*, vol. 109, pp. 398-412, 1986.
- [39] K. Ishimi, H. Hikita, and M. Esmail, "Dynamic contact angles on moving plates," *AIChE journal*, vol. 32, pp. 486-492, 1986.
- [40] P. Sheng and M. Zhou, "Immiscible-fluid displacement: Contact-line dynamics and the velocity-dependent capillary pressure," *Physical Review A*, vol. 45, p. 5694, 1992.
- [41] E. Rillaerts and P. Joos, "The dynamic contact angle," *Chemical Engineering Science*, vol. 35, pp. 883-887, 1980.

- [42] J. Stokes, M. Higgins, A. Kushnick, S. Bhattacharya, and M. O. Robbins, "Harmonic generation as a probe of dissipation at a moving contact line," *Physical review letters*, vol. 65, p. 1885, 1990.
- [43] Y. Zhang, "Static and Dynamic Behaviour of Inter-granular Liquid Bridges: Hysteresis of Contact Angle and Capillary Forces," University of Sydney, 2016.
- [44] J. E. Seebergh and J. C. Berg, "Dynamic wetting in the low capillary number regime," *Chemical Engineering Science*, vol. 47, pp. 4455-4464, 1992.
- [45] A. M. Karim, J. P. Rothstein, and H. P. Kavehpour, "Experimental study of dynamic contact angles on rough hydrophobic surfaces," *Journal of colloid and interface science*, vol. 513, pp. 658-665, 2018.
- [46] H. Liu, Y. Li, W. E. Krause, O. J. Rojas, and M. A. Pasquinelli, "The soft-confined method for creating molecular models of amorphous polymer surfaces," *The Journal of Physical Chemistry B*, vol. 116, pp. 1570-1578, 2012.
- [47] N. Giovambattista, P. G. Debenedetti, and P. J. Rossky, "Effect of surface polarity on water contact angle and interfacial hydration structure. ," *The Journal of Physical Chemistry B*, vol. 111, pp. 9581-9587, 2007.
- [48] J. T. Hirvi and T. A. Pakkanen, "Molecular dynamics simulations of water droplets on polymer surfaces," *The Journal of chemical physics*, vol. 125, p. 144712, 2006.
- [49] S. Do Hong, M. Y. Ha, and S. Balachandar, "Static and dynamic contact angles of water droplet on a solid surface using molecular dynamics simulation," *Journal of colloid and interface science*, vol. 339, pp. 187-195, 2009.
- [50] J.-Y. Park, M.-Y. Ha, H.-J. Choi, S.-D. Hong, and H.-S. Yoon, "A study on the contact angles of a water droplet on smooth and rough solid surfaces," *Journal of Mechanical Science and Technology*, vol. 25, pp. 323-332, 2011.
- [51] D. Sergi, G. Scocchi, and A. Ortona, "Molecular dynamics simulations of the contact angle between water droplets and graphite surfaces," *Fluid Phase Equilibria*, vol. 332, pp. 173-177, 2012.
- [52] J. Chen, B. J. Hanson, and M. A. Pasquinelli, "Molecular Dynamics Simulations for Predicting Surface Wetting," *AIMS Mater. Sci*, vol. 1, pp. 121-131, 2014.
- [53] D. Broesch, "Breaking symmetry in liquid bridges: the effect of pinning and aspect ratio on capillary forces," 2014.
- [54] H. Chen, T. Tang, and A. Amirfazli, "Effects of surface wettability on fast liquid transfer," *Physics of Fluids*, vol. 27, p. 112102, 2015.
- [55] B. Mielniczuk, M. S. El Youssoufi, L. Sabatier, and T. Hueckel, "Rupture of an evaporating liquid bridge between two grains," *Acta Geophysica*, vol. 62, pp. 1087-1108, 2014.
- [56] J. Zhuang and Y. S. Ju, "A combined experimental and numerical modeling study of the deformation and rupture of axisymmetric liquid bridges under coaxial stretching," *Langmuir*, vol. 31, pp. 10173-10182, 2015.
- [57] M. T. Rahni, M. Karbaschi, and R. Miller, *Computational methods for complex liquid-fluid interfaces* vol. 5: CRC Press, 2015.
- [58] R. A. Gingold and J. J. Monaghan, "Smoothed particle hydrodynamics: theory and application to non-spherical stars," *Monthly notices of the royal astronomical society*, vol. 181, pp. 375-389, 1977.
- [59] L. B. Lucy, "A numerical approach to the testing of the fission hypothesis," *The astronomical journal*, vol. 82, pp. 1013-1024, 1977.
- [60] B. Cartwright, P. Groenenboom, and D. McGuckin, "Examples of ship motion and wash predictions by smoothed particle hydrodynamics (sph)," in *9th symposium on practical design of ships and other floating structures, Luebeck-Travemuende, Germany*, 2004.

- [61] X. Y. Hu and N. A. Adams, "A multi-phase SPH method for macroscopic and mesoscopic flows," *Journal of Computational Physics*, vol. 213, pp. 844-861, 2006.
- [62] A. M. Tartakovsky, K. F. Ferris, and P. Meakin, "Lagrangian particle model for multiphase flows," *Computer Physics Communications*, vol. 180, pp. 1874-1881, 2009.
- [63] T. D. Scheibe, Z. Hou, B. J. Palmer, and A. M. Tartakovsky, "Pore - scale simulation of intragranular diffusion: Effects of incomplete mixing on macroscopic manifestations," *Water Resources Research*, vol. 49, pp. 4277-4294, 2013.
- [64] J. J. Monaghan, "Smoothed particle hydrodynamics," *Reports on progress in physics*, vol. 68, p. 1703, 2005.
- [65] J. J. Monaghan, "Smoothed particle hydrodynamics," *Annual review of astronomy and astrophysics*, vol. 30, pp. 543-574, 1992.
- [66] P. Mostaghimi, B. S. Tollit, S. J. Neethling, G. J. Gorman, and C. C. Pain, "A control volume finite element method for adaptive mesh simulation of flow in heap leaching," 2014.
- [67] J. J. Monaghan, "SPH without a tensile instability," *Journal of Computational Physics*, vol. 159, pp. 290-311, 2000.
- [68] J. J. Monaghan, "An introduction to SPH," *Computer physics communications*, vol. 48, pp. 89-96, 1988.
- [69] R. Gingold and J. Monaghan, "Kernel estimates as a basis for general particle methods in hydrodynamics," *Journal of Computational Physics*, vol. 46, pp. 429-453, 1982.
- [70] G. Oger, M. Doring, B. Alessandrini, and P. Ferrant, "An improved SPH method: Towards higher order convergence," *Journal of Computational Physics*, vol. 225, pp. 1472-1492, 2007.
- [71] P. Mostaghimi, I. S. K. Ilankoon, and S. J. Neethling, "Use of mesh adaptivity in simulation of flow in packed beds—A case study," *Minerals Engineering*, vol. 63, pp. 157-163, 2014.
- [72] Y. Zhu, P. J. Fox, and J. P. Morris, "A pore - scale numerical model for flow through porous media," *International journal for numerical and analytical methods in geomechanics*, vol. 23, pp. 881-904, 1999.
- [73] J. Brackbill, D. B. Kothe, and C. Zemach, "A continuum method for modeling surface tension," *Journal of computational physics*, vol. 100, pp. 335-354, 1992.
- [74] F. Yeganehdoust, M. Yaghoubi, H. Emdad, and M. Ordoubadi, "Numerical study of multiphase droplet dynamics and contact angles by smoothed particle hydrodynamics," *Applied Mathematical Modelling*, vol. 40, pp. 8493-8512, 2016.
- [75] S. Adami, X. Hu, and N. Adams, "A new surface-tension formulation for multi-phase SPH using a reproducing divergence approximation," *Journal of Computational Physics*, vol. 229, pp. 5011-5021, 2010.
- [76] A. Tartakovsky and P. Meakin, "Modeling of surface tension and contact angles with smoothed particle hydrodynamics," *Physical Review E*, vol. 72, p. 026301, 2005.
- [77] M. Becker and M. Teschner, "Weakly compressible SPH for free surface flows," in *Proceedings of the 2007 ACM SIGGRAPH/Eurographics symposium on Computer animation*, 2007, pp. 209-217.
- [78] H. Hochstetter and A. Kolb, "Evaporation and condensation of SPH-based fluids," in *Proceedings of the ACM SIGGRAPH/Eurographics Symposium on Computer Animation*, 2017, p. 3.
- [79] A. Farrokhpahan, "Applying Contact Angle to a Two-Dimensional Smoothed Particle Hydrodynamics (SPH) model on a Graphics Processing Unit (GPU) Platform," *Master's thesis, University of Toronto, Toronto, ON, Canada*, 2012.
- [80] G.-R. Liu and M. B. Liu, *Smoothed particle hydrodynamics: a meshfree particle method*: World Scientific, 2003.

- [81] R. A. Dalrymple and B. D. Rogers, "Numerical modeling of water waves with the SPH method," *Coastal engineering*, vol. 53, pp. 141-147, 2006.
- [82] J. J. Monaghan and A. Kos, "Solitary waves on a Cretan beach," *Journal of waterway, port, coastal, and ocean engineering*, vol. 125, pp. 145-155, 1999.
- [83] D. Violeau and R. Issa, "Numerical modelling of complex turbulent free - surface flows with the SPH method: an overview.," *International Journal for Numerical Methods in Fluids*, vol. 53, pp. 277-304, 2007.
- [84] A. Vorobyev, *A Smoothed particle hydrodynamics method for the simulation of centralized sloshing experiments*: KIT Scientific Publishing, 2012.
- [85] J. P. Morris, P. J. Fox, and Y. Zhu, "Modeling low Reynolds number incompressible flows using SPH," *Journal of computational physics*, vol. 136, pp. 214-226, 1997.
- [86] S. Adami, X. Y. Hu, and N. A. Adams, "A transport-velocity formulation for smoothed particle hydrodynamics," *Journal Of Computational Physics*, vol. 241, pp. 292-307, May 2013.
- [87] M. Meister, G. Burger, and W. Rauch, "On the Reynolds number sensitivity of smoothed particle hydrodynamics," *Journal of Hydraulic Research*, vol. 52, pp. 824-835, 2014.
- [88] J. Monaghan, "On the problem of penetration in particle methods," *Journal of Computational physics*, vol. 82, pp. 1-15, 1989.
- [89] L. Li, L. Shen, G. D. Nguyen, A. El-Zein, and F. Maggi, "A smoothed particle hydrodynamics framework for modelling multiphase interactions at meso-scale," *Computational Mechanics*, pp. 1-15, 2018.
- [90] J. J. Monaghan and J. B. Kajtár, "SPH particle boundary forces for arbitrary boundaries," *Computer Physics Communications*, vol. 180, pp. 1811-1820, 2009.
- [91] A. Colagrossi and M. Landrini, "Numerical simulation of interfacial flows by smoothed particle hydrodynamics," *Journal of Computational Physics*, vol. 191, pp. 448-475, 2003.
- [92] J. Feldman and J. Bonet, "Dynamic refinement and boundary contact forces in SPH with applications in fluid flow problems," *International Journal for Numerical Methods in Engineering*, vol. 72, pp. 295-324, 2007.
- [93] J. Wang and D. Chan, "Frictional contact algorithms in SPH for the simulation of soil-structure interaction," *International Journal for Numerical and Analytical Methods in Geomechanics*, vol. 38, pp. 747-770, 2014.
- [94] P. Ramachandran, "PySPH: a reproducible and high-performance framework for smoothed particle hydrodynamics," in *Proceedings of the 15th Python in Science Conference*, 2016, pp. 127-135.
- [95] B. J. Kirby, *Micro-and nanoscale fluid mechanics: transport in microfluidic devices*: Cambridge University Press, 2010.
- [96] A. Niavarani and N. V. Priezjev, "Modeling the combined effect of surface roughness and shear rate on slip flow of simple fluids," *Physical Review E*, vol. 81, p. 011606, 2010.
- [97] X. Li, X. Fan, A. Askounis, K. Wu, K. Sefiane, and V. Koutsos, "An experimental study on dynamic pore wettability," *Chemical Engineering Science*, vol. 104, pp. 988-997, 2013.
- [98] Z. Shi, Y. Zhang, M. Liu, D. A. Hanaor, and Y. Gan, "Dynamic contact angle hysteresis in liquid bridges," *arXiv preprint arXiv:1712.04703*, 2017.
- [99] J. P. Hughes and D. I. Graham, "Comparison of incompressible and weakly-compressible SPH models for free-surface water flows," *Journal of Hydraulic Research*, vol. 48, pp. 105-117, 2010.

- [100] E. Gatapova and A. Novikova, "Evolution of liquid bridge rupture in the evaporator model," in *EPJ Web of Conferences*, 2017, p. 00021.
- [101] C.-H. Huang, M. S. Carvalho, and S. Kumar, "Stretching liquid bridges with moving contact lines: comparison of liquid-transfer predictions and experiments," *Soft matter*, vol. 12, pp. 7457-7469, 2016.
- [102] H. Chen, T. Tang, and A. Amirfazli, "Fast liquid transfer between surfaces: breakup of stretched liquid bridges," *Langmuir*, vol. 31, pp. 11470-11476, 2015.
- [103]

Appendix A:

2D Hagen–Poiseuille equation derivation

Firstly, we consider a solid cylinder of fluid, with radius r inside a hollow cylindrical pipe of radius R , as shown in Fig. A.

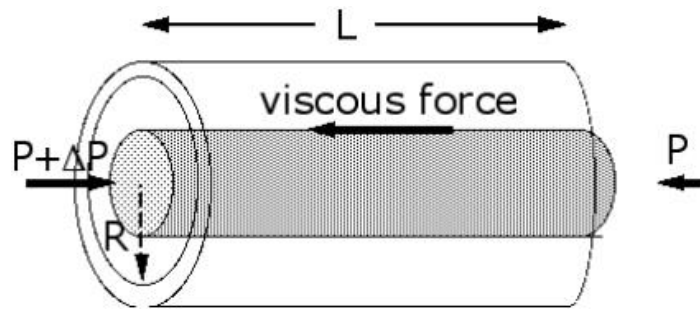


Fig. A. Pressure-driven fluid inside a cylinder [103].

In an equilibrium condition of constant speed, the net force goes to zero.

$$F_{pressure} + F_{viscosity} = 0,$$

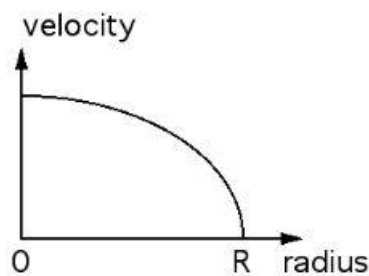
$$\Delta p \cdot A = 0,$$

$$\Delta p \cdot 2r = \eta L \frac{dv}{dr}.$$

So

$$\frac{dv}{dr} = \frac{\Delta p \cdot 2r}{\eta L}.$$

Empirically, the velocity gradient is like the figure below.



At the centre: when $r = 0$: $\frac{dv}{dr} = 0$, v reaches maximum; when $r = R$: $v = 0$. From the velocity gradient equation above and the empirical velocity gradient limits, an integration can be made to get an expression for the velocity

$$\frac{dv}{dr} = \left(\frac{2\Delta p}{\eta L} \right) r.$$

Rewriting:

$$\int_v^0 dv = \left(\frac{2\Delta p}{\eta L} \right) \cdot \int_r^R r dr,$$

$$v(r) = \left(\frac{\Delta p}{\eta L} \right) \cdot [R^2 - r^2].$$

Now, the equation of continuity giving the volume flux for a variable speed is:

$$\frac{dV}{dt} = \int v \cdot dA.$$

Substituting the velocity profile equation and the surface area of the moving cylinder:

$$\begin{aligned} \frac{dV}{dt} &= \int_0^R \left(\frac{\Delta p}{\eta L} \right) \cdot [R^2 - r^2] dr \\ &= \left(\frac{\Delta p}{\eta L} \right) \int_0^R \left[R^2 r - \frac{1}{3} r^3 \right] \\ &= \frac{2}{3} R^3 \cdot \left(\frac{\Delta p}{\eta L} \right). \end{aligned}$$

In 2D case, $\frac{dV}{dt} = A \cdot v = 2Rv$

So the final expression for viscosity is:

$$\eta = \frac{\Delta p R^2}{3Lv}.$$

Appendix B:

Image processing for contact angle fitting

In this appendix section, the capillary tube image is processed and the contact angle at triple-line region is fitted. The script is written in Wolfram Mathematica 10.3.

```
ClearAll[process]

process[Data_] := Module[{img, pts, s1, line1, a}, img = Dilation[Data, DiskMatrix[5]];
  img = Binarize[img, 0.67];
  img = CurvatureFlowFilter[img, 10];
  img = EdgeDetect[img, 10];
  img = RemoveAlphaChannel[ColorNegate@ColorConvert[img, "Grayscale"]];
  pts = PixelValuePositions[img, Black, .2];
  s1 = Select[pts, 50 > #[[1]] > 0 &];
  line1 = Fit[s1, {1, x}, x];
  a = Coefficient[line1, x ^ 1];
  a = ArcTan[a] * 180 / 3.1415926545;
  a = 90 + a]

files = FileNames["*.jpg", NotebookDirectory[]];
images = Import[#] & /@ files
results = process /@ images
results // TableForm
Export["advancing01.xlsx", results]
```

Appendix C: Liquid particle counting

In this section, the liquid bridge image is processed and the number of liquid particle is counted.

```
img = Import["desktop/LiquidBridge01.jpg"]
img = FillingTransform[ColorNegate[Binarize[img, 0.3]]]
distT = DistanceTransform[img, Padding -> 0]
marker = MaxDetect[ImageAdjust[distT], 0.01]
w = WatershedComponents[GradientFilter[img, 5.5], marker, Method -> "Rainfall"];
Colorize[w]
cells = SelectComponents[w, "Count", 0 < # < 3000 &];
measures = ComponentMeasurements[cells, {"Centroid", "EquivalentDiskRadius", "Label"}];
Style["Number of Cell is " <> ToString[Dimensions[measures][[1]]] <> ".", "Title"]
```